Monthly Notices
of the
ROYAL ASTRONOMICAL SOCIETY

Mon. Not. R. Astron. Soc. **421,** 1982–1995 (2012) doi:10.1111/j.1365-2966.2012.20415.x

# Characterization of the non-Gaussianity of radio and IR point sources at CMB frequencies

F. Lacasa,[1⋆] N. Aghanim,[1] M. Kunz[2] and M. Frommert[2]

[1]*Institut d'Astrophysique Spatiale (IAS), Bâtiment 121, F-91405 Orsay, Université Paris-Sud 11 and CNRS, UMR 8617, France*
[2]*Département de Physique Théorique and Center for Astroparticle Physics, Université de Genève, 24 quai E. Ansermet, Genève, Switzerland*

Accepted 2011 December 19. Received 2011 December 12; in original form 2011 July 11

**ABSTRACT**

This study, using publicly available simulations, focuses on the characterization of the non-Gaussianity produced by radio point sources and by infrared (IR) sources in the frequency range of the cosmic microwave background from 30 to 350 GHz.

We propose a simple prescription to infer the angular bispectrum from the power spectrum of point sources considering independent populations of sources, with or without clustering. We test the accuracy of our prediction using publicly available all-sky simulations of radio and IR sources and find very good agreement.

We further characterize the configuration dependence and the frequency behaviour of the IR and radio bispectra. We show that the IR angular bispectrum peaks for squeezed triangles and that the clustering of IR sources enhances the bispectrum values by several orders of magnitude at scales $\ell \sim 100$. At 150 GHz the bispectrum of IR sources starts to dominate that of radio sources on large angular scales, and it dominates the whole multipole range at 350 GHz.

Finally, we compute the bias on $f_{\rm NL}$ induced by radio and IR sources. We show that the positive bias induced by radio sources is significantly reduced by masking the sources. We also show, for the first time, that the form of the IR bispectrum mimics a primordial 'local' bispectrum $f_{\rm NL}$. The IR sources produce a negative bias which becomes important for *Planck*-like resolution and at high frequencies ($\Delta f_{\rm NL} \sim -6$ at 277 GHz and $\Delta f_{\rm NL} \sim -60$–$70$ at 350 GHz). Most of the signal being due to the clustering of faint IR sources, the bias $\Delta f_{\rm NL}^{\rm IR}$ is not reduced by masking sources above a flux limit and may, in some cases, even be increased due to the reduction of the shot-noise term.

**Key words:** methods: statistical – galaxies: statistics – cosmic background radiation – large-scale structure of Universe – infrared: galaxies – radio continuum: galaxies.

## 1 INTRODUCTION

In the last few decades, the cosmic microwave background (CMB) has become a very successful probe of the early and late Universe. The smallness of the perturbations in the cosmic fluids, and hence in the space–time metric, allows us to use linear perturbation theory to compute their evolution efficiently and accurately through Boltzmann codes (Seljak & Zaldarriaga 1996; Lewis, Challinor & Lasenby 2000; Lesgourgues 2011).

Since *COBE* (Smoot et al. 1992) the measurement of the CMB power spectrum has been achieved by many experiments and over a wide range of scales. The most recent CMB data are those of the seven-year *Wilkinson Microwave Anisotropy Probe* (*WMAP*) (Larson et al. 2011), Atacama Cosmology Telescope (ACT) (Barrientos et al. 2010) and South Pole Telescope (SPT) (Keisler et al. 2011). Constraints from all these measurements, combined with probes of the geometry of the Universe, like baryonic acoustic oscillations (e.g. Percival et al. 2010; Blake et al. 2011), Type Ia supernovae (e.g. Astier et al. 2006; Hicken et al. 2009; Guy et al. 2010) and *Hubble* constant measurements (e.g. Freedman et al. 2001, 2009; Riess et al. 2009), give a converging view of our Universe and have led to the establishment of a 'standard model' of cosmology (e.g. Larson et al. 2011) known as $\Lambda$ cold dark matter ($\Lambda$CDM). In this model, the universe is flat, dominated by a CDM component and a 'dark energy' component compatible with a cosmological constant. The present constraints suggest that CMB anisotropies are a realization of a primordial random process that generated the initial perturbations from quantum fluctuations which were then stretched to macroscopic scales by inflation (e.g. Starobinskiĭ 1979;

⋆E-mail: Fabien.Lacasa@ias.u-psud.fr

Guth 1981; Liddle & Lyth 2000, see also Bassett, Tsujikawa & Wands 2006; Linde 2008, for reviews).

The microwave sky is however not made of a CMB primary signal alone; it also consists of secondary anisotropies such as those associated with the integrated Sachs–Wolfe effect (ISW) – arising from the time-variable metric perturbations (Sachs & Wolfe 1967) – those arising from the Sunyaev–Zel'dovich (SZ) effect (inverse Compton scattering) in the direction of galaxy clusters (Sunyaev & Zeldovich 1972) and those due to the Doppler effect from moving structures (e.g. kinetic SZ effect from clusters and inhomogeneous reionization), see Aghanim, Majumdar & Silk (2008) for a review on secondary anisotropies. In addition, there are other astrophysical components in the microwave domain such as the dust, synchrotron and free–free emissions from our Galaxy (Planck Collaboration 2011e), the emission from radio sources that dominate at lower frequencies but contribute significantly at microwave frequencies (de Zotti et al. 2005) and the emission from dusty star-forming galaxies emitting mainly in the infrared (IR) domain (Low & Tucker 1968).

In this study, we will focus only on the characterization of the extragalactic point sources, namely the radio sources and the IR dusty galaxies. They contribute notably to the power spectrum at CMB frequencies and start dominating the CMB at about $\ell \sim 2000$ when the CMB signal plummets. Active galactic nuclei are observed as radio sources via their synchrotron emission. They have been widely studied in the CMB context especially at low frequencies $\nu \leq 90$ GHz (e.g. de Zotti et al. 2005; Boughn & Partridge 2008; Sajina et al. 2011). They affect mostly the lower end of frequencies observed by CMB experiments. Their largest impact was thought to be in the frequency bands from 30 to 90 GHz but the recent *Planck* results (Planck Collaboration 2011a,c) show that radio sources are detected at frequencies as high as 217 GHz. At the CMB frequencies, radio sources do not cluster (Toffolatti et al. 1998; González-Nuevo, Toffolatti & Argüeso 2005) and thus exhibit a flat power spectrum (see Appendix A).

Star-forming galaxies are observed as IR sources via the thermal emission from dust heated by the ultraviolet emission of young stars. These IR sources contribute to the signal observed by CMB experiments at frequencies higher than 150 GHz; thus, they are particularly relevant for the most recent CMB experiments, e.g. SPT, ACT and *Planck* High Frequency Instrument observations. The cumulated emission from the IR sources, the cosmic infrared background (CIB), was first discovered by Puget et al. (1996), and its anisotropies were first characterized by Lagache & Puget (2000) and Matsuhara et al. (2000). Many other observations were possible in the last decade in the IR and submillimetre domain (Lagache et al. 2007; Viero et al. 2009; Hall et al. 2010; Amblard et al. 2011; Planck Collaboration 2011d). In particular, the latest constraints of the CIB from *Planck* showed that its power spectrum, at frequencies 217, 353, 545 and 857 GHz, is well modelled by a power law $C_\ell^{\rm CIB}(\nu) = A(\nu) \times \left(\frac{\ell}{1000}\right)^n$ with e.g. $A = (104 \pm 4) \times 10^2\,{\rm Jy^2\,sr^{-1}}$ and $n = -1.08 \pm 0.06$ at 545 GHz. This behaviour contrasts with the flat spectrum of radio sources and is due to the clustering of the IR galaxies and their host dark matter (DM) haloes.

These point sources are superimposed on the primordial fluctuations. The simplest models of inflation (single field and slow roll) predict a small primordial non-Gaussianity (NG) (Acquaviva et al. 2003; Maldacena 2003; Creminelli & Zaldarriaga 2004) that is subdominant to the NG induced by the non-linear evolution of the perturbations, a contribution that is necessarily always present. More complex inflationary models, e.g. multi-field scenarios, may predict larger NG (Byrnes & Choi 2010), to the point of being detectable. A simple and yet powerful probe of NG is the three-point function in harmonic space, the angular bispectrum (see Section 2 for more details), which is defined as a function of a multipole triplet $(\ell_1, \ell_2, \ell_3)$. The angular bispectrum vanishes for a Gaussian field like all odd-order moments. Besides the bispectrum, connected even-order moments may also be used to probe NG and the four-point function or trispectrum has indeed been a focus of interest (Kunz et al. 2001), especially for lensing studies (Cooray & Kesden 2002).

There are many different models of inflation, and they often predict very similar power spectra that are close to being scale invariant. For models that lead to a measurable bispectrum, however, this degeneracy can often be broken by studying the dependence of the bispectrum amplitude on $(\ell_1, \ell_2, \ell_3)$, e.g., a large signal for squeezed triangles is indicative of slow-roll multifield inflation models, equilateral triangles are enhanced for models with non-canonical kinetic terms and folded triangles for non-standard vacuum initial conditions (e.g. Bartolo et al. 2004; Renaux-Petel 2009; Lewis 2011). The most studied and constrained form of NG is the local ansatz parametrized by a factor $f_{\rm NL}$, and predicted by several inflation models. Current constraints on local NG show that the CMB is consistent with being Gaussian at the 95 per cent CL (Komatsu et al. 2011), and constraints on other shapes all show consistency with Gaussianity as well.

Given the current limits on primordial NG, astrophysical signals are the dominant contribution to NG. While Galactic emission and resolved sources may be accounted for by masking, unresolved sources and residuals have to be characterized. As opposed to primordial NG, radio sources' NG has been detected, and was studied for the *WMAP* mission showing that it yields a non-zero flat angular bispectrum parametrized as $b_{\rm src}$ or $b_{\rm ps}$. The fiveyear *WMAP* best estimate in the $Q$ band is $b_{\rm src} = 4.3 \pm 1.3\,\mu{\rm K^3\,sr^2}$ (Komatsu et al. 2009). Characterizing the NG signal from astrophysical components and more importantly from extragalactic point sources is important for two main reasons: (i) to avoid mistaking it for a primordial contribution (and to allow the development of robust methods to isolate primordial NG) and (ii) to learn more about astrophysical processes, i.e. to go beyond the description of point sources by their number counts and their power spectrum.

The study of NG from extragalactic point sources has been pioneered by Argueso, Gonzalez-Nuevo & Toffolatti (2003), focusing mostly on the radio sources and including clustering. They showed that the point-source angular bispectrum is mostly flat at *WMAP* frequencies and dominates the CMB bispectrum in most configurations. Babich & Pierpaoli (2008) investigated the bias on the $f_{\rm NL}$ estimator induced by radio sources, considering the modulation of their number density with ISW, of their magnification with lensing and of the flux cut-off with selection effects. Serra & Cooray (2008) studied the bias on $f_{\rm NL}$ due to radio sources, SZ-lensing and ISW-lensing bispectra, investigating the dependence of this bias with the resolution scale. Finally, Munshi et al. (2009) defined skew spectra for cross-correlation analysis, derived estimators for the skew spectra and applied them to secondary anisotropies.

In this paper, we study the NG produced by infrared and radio point sources in the frequency range of the CMB from 30 to 350 GHz, based on numerical simulations by Sehgal et al. (2010). We investigate the frequency and configuration dependence of the angular bispectrum. We particularly focus on the NG from IR sources and their clustering term. We restrict the study to the simplest case of full-sky maps without masks. Furthermore, we do not take into account noise and beam effects. Statistical isotropy of all fields

considered will be assumed throughout this paper. The case of noisy, partially masked maps will be addressed in future studies.

In Section 2, we review the estimator of the (binned) angular bispectrum and $f_{\rm NL}$ and develop a parametrization of the bispectrum to display and visualize it efficiently. In Section 3, we develop a prescription to infer the bispectrum from the power spectrum for clustered sources and for different populations. In Section 4, we use publicly available full-sky simulations of radio and infrared sources to compute and characterize their bispectrum at CMB frequencies and we compare them to the predictions from the prescription. We examine the configuration dependence of the point-source bispectra and study the bias they induce on the estimation of the primordial local NG in Section 5. We finally conclude and discuss our results in Section 6.

## 2 THREE-POINT NG ESTIMATORS

### 2.1 Full-sky angular bispectrum estimator

Given a full-sky map of the temperature fluctuations $\Delta T(\boldsymbol{n})$ of some signal, it can be decomposed in the spherical harmonic basis

$$a_{\ell m} = \int \mathrm{d}^2\boldsymbol{n}\; Y^*_{\ell m}(\boldsymbol{n})\; \Delta T(\boldsymbol{n}) \tag{1}$$

with the usual orthonormal spherical harmonics $Y_{\ell m}$,

$$\int \mathrm{d}^2\boldsymbol{n}\; Y_{\ell m}(\boldsymbol{n})\; Y^*_{\ell' m'}(\boldsymbol{n}) \;=\; \delta_{\ell\ell'}\,\delta_{mm'}.$$

Observational data are pixelized, so that the integral is replaced by a sum over pixels. We will assume that the solid angle of a pixel, $\Omega_{\rm pix}$, is a constant, which is for example the case for the HEALPIX[1] pixelization scheme that we will adopt for the numerical calculations. In this case we have

$$a_{\ell m} = \sum_{\boldsymbol{n}_i}\; Y^*_{\ell m}(\boldsymbol{n}_i)\; \Delta T(\boldsymbol{n}_i)\, \Omega_{\rm pix}\,. \tag{2}$$

This discreteness effect will be important e.g. in Section 3.1.

In order to compute the angular bispectrum, which is the harmonic transform of the three-point correlation function, we will resort to scale maps as defined by Spergel & Goldberg (1999) and also used by Aghanim et al. (2003) and De Troia et al. (2003):

$$T_\ell(\boldsymbol{n}) = \sum_m a_{\ell m} Y_{\ell m}(\boldsymbol{n}) = \int \mathrm{d}^2\boldsymbol{n}'\; \Delta T(\boldsymbol{n}')\; P_\ell(\boldsymbol{n}\cdot\boldsymbol{n}'), \tag{3}$$

where $P_\ell$ is the Legendre polynomial of order $\ell$.

The optimal bispectrum estimator is then (Spergel & Goldberg 1999)

$$\hat{b}_{\ell_1\ell_2\ell_3} = \frac{4\pi}{(2\ell_1+1)(2\ell_2+1)(2\ell_3+1)} \begin{pmatrix} \ell_1 & \ell_2 & \ell_3 \\ 0 & 0 & 0 \end{pmatrix}^{-2} \times \int \mathrm{d}^2\boldsymbol{n}\; T_{\ell_1}(\boldsymbol{n})\, T_{\ell_2}(\boldsymbol{n})\, T_{\ell_3}(\boldsymbol{n}) \tag{4}$$

or it can be written in the form

$$\hat{b}_{\ell_1\ell_2\ell_3} = \sqrt{\frac{4\pi}{(2\ell_1+1)(2\ell_2+1)(2\ell_3+1)}} \begin{pmatrix} \ell_1 & \ell_2 & \ell_3 \\ 0 & 0 & 0 \end{pmatrix}^{-1} \times \sum_{m_1,m_2,m_3} \begin{pmatrix} \ell_1 & \ell_2 & \ell_3 \\ m_1 & m_2 & m_3 \end{pmatrix} a_{\ell_1 m_1}\, a_{\ell_2 m_2}\, a_{\ell_3 m_3}, \tag{5}$$

[1] http://healpix.jpl.nasa.gov

where the expression in brackets represents the Wigner 3$j$ symbols. Equation (5) is computationally expensive when implemented at high $\ell$ due to the large number of Wigner symbols to calculate. Equation (4) still requires a few cpu-days for a full computation at a *Planck*-like resolution, Nside = 1024–2048. Binning the multipoles in $\ell$, as in Bucher, Tent & Carvalho (2010), has the advantage of speeding up the computations and smoothing out the variations due to cosmic variance.

For a given triangle in harmonic space $(\ell_1, \ell_2, \ell_3)$ the number of independent configurations on the sphere is

$$N_{\ell_1\ell_2\ell_3} = \frac{(2\ell_1+1)(2\ell_2+1)(2\ell_3+1)}{4\pi} \begin{pmatrix} \ell_1 & \ell_2 & \ell_3 \\ 0 & 0 & 0 \end{pmatrix}^2. \tag{6}$$

When multipoles are binned in bins of width $\Delta\ell$ the expression for the scale maps (equation 3) becomes

$$T_{\Delta\ell}(\boldsymbol{n}) = \sum_{\ell\in\Delta\ell,m} a_{\ell m}\, Y_{\ell m}(\boldsymbol{n}) \tag{7}$$

and a binned bispectrum estimator identically weighting triangles is given by

$$\hat{b}_{\Delta\ell_1,\Delta\ell_2,\Delta\ell_3} = \frac{1}{N_\Delta(\Delta\ell_1,\Delta\ell_2,\Delta\ell_3)} \int \mathrm{d}^2\boldsymbol{n}\; T_{\Delta\ell_1}(\boldsymbol{n})\, T_{\Delta\ell_2}(\boldsymbol{n})\, T_{\Delta\ell_3}(\boldsymbol{n}), \tag{8}$$

where

$$N_\Delta(\Delta\ell_1,\Delta\ell_2,\Delta\ell_3) = \sum_{\ell_i\in\Delta\ell_i} N_{\ell_1\ell_2\ell_3}.$$

One can easily check that the obtained binned bispectrum estimator is unbiased for a constant bispectrum and that the bias can be neglected as long as the bispectrum does not vary significantly within a bin $\Delta\ell$. In the following, we have chosen $\ell_{\rm max} = 2048$ and a bin width $\Delta\ell = 64$ for simplicity and computational speed while retaining enough information on the scale dependence (Bucher et al. 2010).

### 2.2 $f_{\rm NL}$ estimator

The most studied and constrained form of primordial NG is the local ansatz, whose amplitude is parametrized by a non-linear coupling constant $f_{\rm NL}$:

$$\Phi(\boldsymbol{x}) = \Phi_{\rm G}(\boldsymbol{x}) + f_{\rm NL}\left(\Phi^2_G(\boldsymbol{x}) - \langle\Phi^2_{\rm G}(\boldsymbol{x})\rangle\right), \tag{9}$$

where $\Phi(\boldsymbol{x})$ is the Bardeen potential and $\Phi_{\rm G}(\boldsymbol{x})$ is a Gaussian field. This form of NG yields the following CMB angular bispectrum (Komatsu & Spergel 2001):

$$b^{\rm loc}_{\ell_1\ell_2\ell_3} = \int r^2\,\mathrm{d}r\;\alpha_{\ell_1}(r)\,\beta_{\ell_2}(r)\,\beta_{\ell_3}(r) + \text{permutation}, \tag{10}$$

with

$$\alpha_\ell(r) = \frac{2}{\pi}\int k^2\mathrm{d}k\; g_{{\rm T},\ell}(k)\; j_\ell(kr) \tag{11}$$

$$\beta_\ell(r) = \frac{2}{\pi}\int k^2\mathrm{d}k\; P(k)\; g_{T,\ell}(k)\; j_\ell(kr), \tag{12}$$

where $g_{{\rm T},\ell}$ is the radiation transfer function, which can be computed with a Boltzmann code, $j_\ell$ are the spherical Bessel functions and $P(k) \propto k^{n_{\rm s}-4}$ is the primordial power spectrum, with a spectral index $n_{\rm s}$.

On large angular scales, the SW effect is the dominant contribution to the CMB signal. In this regime, the CMB bispectrum takes the following analytical form:

$$b^{\rm loc}_{\ell_1\ell_2\ell_3} \propto -\left(\frac{1}{\ell_1^2\,\ell_2^2} + \frac{1}{\ell_1^2\,\ell_3^2} + \frac{1}{\ell_2^2\,\ell_3^2}\right). \tag{13}$$

This bispectrum is maximal when one of the multipoles is minimal ($\ell_1 \ll \ell_2 \simeq \ell_3$) which is called the squeezed configuration.

A commonly used cubic estimator of $f_{\rm NL}$ has been developed by Komatsu, Spergel & Wandelt (2005). It is much faster than performing the whole bispectrum analysis and fitting the local bispectrum. In its original version, the estimator takes into account beam profile and homogeneous noise, and has been used on *WMAP* data to yield the current constraint $-10 < f_{\rm NL} < 74$ (Komatsu et al. 2011). The estimator was then further developed by several authors by adding a linear term accounting for masking and inhomogeneous noise (Creminelli et al. 2006). Here, we will only consider noiseless full-sky maps without beam smoothing so that we can apply the estimator in its original form.

To build the $f_{\rm NL}$ estimator we first define the filtered maps at comoving distance $r$ and direction $\boldsymbol{n}$:

$$A(r,\boldsymbol{n}) = \sum_{\ell m} \frac{\alpha_\ell(r)}{C_\ell}\, a_{\ell m}\, Y_{\ell m}(\boldsymbol{n}) \tag{14}$$

$$B(r,\boldsymbol{n}) = \sum_{\ell m} \frac{\beta_\ell(r)}{C_\ell}\, a_{\ell m}\, Y_{\ell m}(\boldsymbol{n}), \tag{15}$$

where $C_\ell$ is the CMB power spectrum. $B(r,\boldsymbol{n})$ is then an estimated map of the primordial potential fluctuations $\Phi(r\ \boldsymbol{n})$ via Wiener filtering.

The integral of $AB^2$ permits us to estimate $f_{\rm NL}$ as

$$\hat{f}_{\rm NL} \sum_{\ell_1\le\ell_2\le\ell_3} \frac{\left(B^{\rm loc}_{\ell_1\ell_2\ell_3}\right)^2}{C_{\ell_1}C_{\ell_2}C_{\ell_3}} = \int r^2 {\rm d}r\, {\rm d}^2\boldsymbol{n}\, A(r,\boldsymbol{n})\, B^2(r,\boldsymbol{n}), \tag{16}$$

where $B^{\rm loc}_{\ell_1\ell_2\ell_3} = \sqrt{N_{\ell_1\ell_2\ell_3}}\, b^{\rm loc}_{\ell_1\ell_2\ell_3}$ is the local bispectrum for $f_{\rm NL} = 1$, to be compared with the observed value $B^{\rm obs}_{\ell_1\ell_2\ell_3}$.

It can be shown that this estimator takes analytically the form

$$\hat{f}_{\rm NL} = \frac{\sum_{\ell_1\le\ell_2\le\ell_3} \frac{B^{\rm obs}_{\ell_1\ell_2\ell_3} B^{\rm loc}_{\ell_1\ell_2\ell_3}}{C_{\ell_1}C_{\ell_2}C_{\ell_3}}}{\sum_{\ell_1\le\ell_2\le\ell_3} \frac{\left(B^{\rm loc}_{\ell_1\ell_2\ell_3}\right)^2}{C_{\ell_1}C_{\ell_2}C_{\ell_3}}}. \tag{17}$$

It is near optimal in the sense that it minimizes the $\chi^2$ for weak NG (under some assumptions on isosceles and equilateral triangles). The estimator becomes suboptimal (e.g. Elsner & Wandelt 2009) for large enough $f_{\rm NL}$, when the variance of the bispectrum gets $O\left(f_{\rm NL}^2\right)$ correction compared to the weak NG computation with Wick's theorem (see Appendix B).

### 2.3 Parametrization of the angular bispectrum

Several ways of visualizing the angular bispectrum have been proposed in the literature, e.g. isosurfaces in the $(\ell_1, \ell_2, \ell_3)$ 3D space by Fergusson & Liguori (2010), or slices of constant perimeter in the orthogonal transverse coordinate $(\ell_{\perp a}, \ell_{\perp b})$ space by Bucher et al. (2010).

Under the assumption of statistical isotropy, the bispectrum $b_{\ell_1\ell_2\ell_3}$ is invariant under permutations of $\ell_1$, $\ell_2$ and $\ell_3$, i.e. it is a function of the shape and size of the triangle $(\ell_1, \ell_2, \ell_3)$ only, i.e. independent of its orientation. Therefore, we can find a parametrization invariant under permutation of $\ell_1$, $\ell_2$ and $\ell_3$, which avoids redundancy of information and allows convenient visualization and interpretation of data. Let us denote as $\overline{(\ell_1, \ell_2, \ell_3)}$ the equivalence class of the triplet under permutations.

The elementary symmetric polynomials ensure the invariance under permutations:

(i) $\sigma_1 = \ell_1 + \ell_2 + \ell_3$

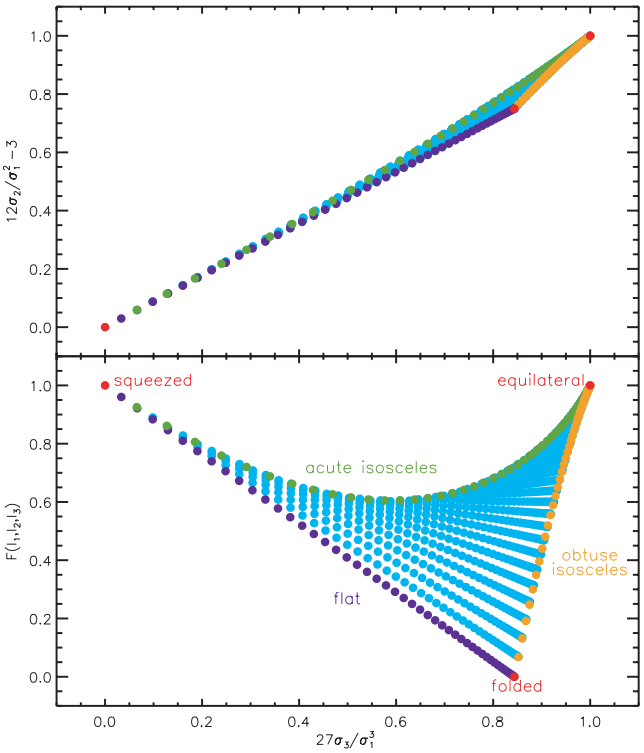


**Figure 1.** Triangles of constant perimeter, $P$, in the parametrization defined by the normalized symmetric polynomials (upper panel), or in the parameter space $(F, S)$ defined in the text (bottom panel).

(ii) $\sigma_2 = \ell_1\ell_2 + \ell_1\ell_3 + \ell_2\ell_3$

(iii) $\sigma_3 = \ell_1\ell_2\ell_3$.

Through Cardan's formula, there is a one-to-one correspondence between $\overline{(\ell_1, \ell_2, \ell_3)}$, defined by the roots of the polynomial $X^3 - \sigma_1 X^2 + \sigma_2 X - \sigma_3$, and the triplet $(\sigma_1, \sigma_2, \sigma_3)$. We further define the scale-invariant parameters $\tilde{\sigma}_2 = 12\sigma_2/\sigma_1^2 - 3$ and $\tilde{\sigma}_3 = 27\sigma_3/\sigma_1^3$ with coefficient chosen so that $\tilde{\sigma}_2$ and $\tilde{\sigma}_3$ vary in the range [0,1]. As illustrated in the upper panel of Fig. 1, this parametrization does not allow us to discriminate efficiently between the different triangles.

We find that the parameters noted $(P, F, S)$ and defined as

(i) $P = \sigma_1$,

(ii) $F = 32(\tilde{\sigma}_2 - \tilde{\sigma}_3)/3 + 1$ and

(iii) $S = \tilde{\sigma}_3$

provide a clearer distinction of the triangles as is illustrated in the bottom panel of Fig. 1.

To illustrate the use of our $(P, F, S)$ parametrization, we plot in Fig. 2[2] the theoretical CMB bispectrum produced by the local NG model $f_{\rm NL}$, computed through equation (10). The triangle perimeters, $P$, vary between $P_{\rm min} = 30$ (equilateral configuration with $\ell_{\rm min} = 10$) and $P_{\rm max} = 6120$ (equilateral configuration with $\ell_{\rm max} = 2040$). We plot representative perimeters tracing the building up of the bispectrum with scale, giving $P/3$ on each panel. The colour code scales from deep purple/black (most negative) to red/dark grey (positive).

In the first panels for the smallest perimeters, few triangles are present. As the perimeter increases the $(F, S)$ space is populated

[2] For space reasons we include only some of the bins in the figures in the paper. Full resolution plots with all perimeter bins are available upon request.

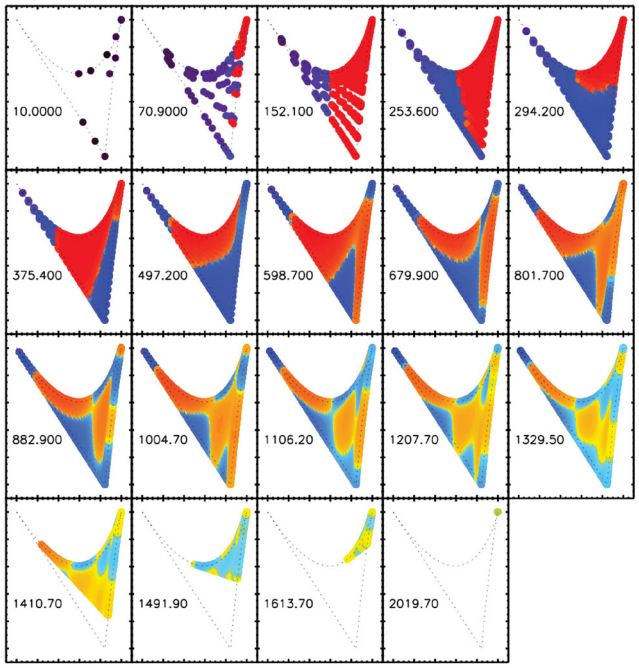


**Figure 2.** Theoretical CMB angular bispectrum produced by the local model in the $(P, F, S)$ parametrization. With chosen representative perimeters and asinh colour scale from deep purple/black (most negative) to red/dark grey (positive). $P/3$ is given on each panel. The axes are the same as those in Fig. 1.

starting with equilateral configurations (upper-right corner) first to reach squeezed configuration (upper-left corner) later. Conversely in the last panels for the largest perimeters, the resolution limit $\ell_{\rm max} = 2048$ limits the possible configurations, leaving only the equilateral triangles in the end.

The SW shape (see equation 13) is visible at low perimeters, with the colours (value of the bispectrum) varying horizontally with $S$ but not vertically with $F$. We note that the strong negative values (deep purple/black) are located in the near-squeezed configuration (upper-left corner). The sign of the radiation transfer function can be traced via the equilateral triangles which are positive for $P/3 \sim 200$ (first acoustic peak) and become negative for $P/3 \sim 500$ (second acoustic peak). The squeezed configuration in turn is always negative as the smallest multipole has a negative transfer function via SW. The folded configuration has relatively large negative values when the two smallest multipoles are in the first acoustic peak while the biggest multipole is in the second acoustic peak ($P \sim 900$–$1200 \Rightarrow P/3 \sim 300$–$400$). For larger perimeters the structure becomes complex as several acoustic peaks intervene.

## 3 PHYSICAL PRESCRIPTION FOR THE POINT-SOURCE ANGULAR BISPECTRUM

In this section we develop a prescription which permits us to predict the (bi)spectrum of point sources, starting from the simplest case of a single randomly distributed population to the case of multiple clustered populations. This is a situation that is encountered in current and future CMB analyses. Indeed until recently, CMB experiments have focused on frequencies where unclustered radio sources are the only dominant kind of point sources, but the CMB is also non-negligible at higher frequencies where an independent population of dusty galaxies becomes important together with the SZ signal of clusters. This is of particular relevance for *Planck* which has a large frequency range covering both populations.

### 3.1 Single-source population: shot-noise contribution

A source with flux $S$ enclosed in a pixel with solid angle $\Omega_{\rm pix}$ yields a temperature variation $\Delta T = k_\nu \frac{S}{\Omega_{\rm pix}}$, where $k_\nu = \frac{\partial B(\nu,T)}{\partial T}|_{T_{\rm CMB}}$, $B(\nu, T)$ is the blackbody spectrum and $T_{\rm CMB}$ is the CMB mean temperature.

As shown in Appendix A the power spectrum of a source population is given by

$$C_\ell = C_\ell^{\rm clust} + C_\ell^{\rm shot}. \tag{18}$$

The discreteness of the sources produces a constant-term spectrum $C_\ell^{\rm shot}$ which is usually named 'Poissonian' because the number of unclustered point sources is driven a priori by Poisson statistics (Sehgal et al. 2010). The shot-noise term reads

$$C_\ell^{\rm shot} = \frac{k_\nu^2}{4\pi} \times \int_0^{S_{\rm cut}} S^2 \frac{{\rm d}n}{{\rm d}S}\,{\rm d}S, \tag{19}$$

where $\frac{{\rm d}n}{{\rm d}S}$ is the differential number counts of sources and $S_{\rm cut}$ is the detection limit, i.e. sources with $S > S_{\rm cut}$ are detected and masked, the rest being unresolved.

The discreteness property of sources, when computing the three-point correlation function, yields a statistically isotropic angular bispectrum constant with $\ell$:

$$b^{\rm shot}_{\ell_1\ell_2\ell_3} = \frac{k_\nu^3}{4\pi} \times \int_0^{S_{\rm cut}} S^3 \frac{{\rm d}n}{{\rm d}S}\,{\rm d}S \tag{20}$$

for $\ell_i \neq 0$. Equations (18), (19) and (20) are derived in more detail in Appendix A.

The case of sources randomly and independently distributed on the sky is that of the radio sources at CMB frequencies. The correlation vanishes and the total (bi)spectrum is equal to the shot-noise (bi)spectrum. The distribution of the sources is that of a white noise entirely characterized by the one-point probability distribution. In this case, equations (19) and (20) for the shot-noise contribution can be reformulated simply in terms of temperature variations where the white-noise spectrum and bispectrum are related to the variance $\sigma^2$ and skewness $\kappa_3$ of $\Delta T$:

$$C_\ell^{\rm white} = \sigma^2\,\Omega_{\rm pix} \tag{21}$$

$$b^{\rm white}_{\ell_1\ell_2\ell_3} = \kappa_3\,\Omega_{\rm pix}^2, \tag{22}$$

with $\sigma^2 = \langle(\Delta T - \langle\Delta T\rangle)^2\rangle$ and $\kappa_3 = \langle(\Delta T - \langle\Delta T\rangle)^3\rangle$.

### 3.2 Single-source population with correlations

The effect of clustering of a single population of sources, namely radio sources, on the bispectrum was pioneered by Argueso et al. (2003) who proposed a prescription to address this issue. The elements entering the prescription are the number counts of sources and a theoretical or observational correlation function $w(\theta)$. Defining

$$P(k)_{\rm clust} = 2\pi \int w(\theta) J_0(k\theta) {\rm d}\theta, \tag{23}$$

where $\theta$ is the distance on the flat patch and $J_0$ the Bessel function of the first kind and of order zero, the prescription is

$$\delta_k({\rm tot}) = \sqrt{\frac{P(k)_{\rm clust} + P(k)_{\rm shot}}{P(k)_{\rm white}}} \times \delta_k({\rm white}), \tag{24}$$

where $\delta_k$ are the Fourier coefficient of the map; 'shot' and 'white' refer, respectively, to the shot-noise and white-noise process. Then Argueso et al. compute the angular bispectrum from simulated square maps based on their prescription.

In our study, we have extended the above-described prescription to analytically derive the full-sky angular bispectrum. The full-sky scale maps read

$$T_\ell^{\rm tot}(\boldsymbol{n}) = \sqrt{\frac{C_\ell^{\rm clust} + C_\ell^{\rm shot}}{C_\ell^{\rm white}}} \times T_\ell^{\rm white}(\boldsymbol{n}),$$

which reduces to equation (24) in the flat-sky approximation $\ell = 2\pi k$, and assuming $P(k)$ does not vary much within a $k$ bin.

So the power spectrum is given by

$$C_\ell^{\rm tot} = C_\ell^{\rm clust} + C_\ell^{\rm shot}.$$

We remind the reader that Argueso et al.'s prescription is specifically made to meet the above relation and that $C_\ell^{\rm shot} = C_\ell^{\rm white} = {\rm const}$.

More interestingly the bispectrum is found to be

$$\begin{aligned} b^{\rm tot}_{\ell_1\ell_2\ell_3} &= \sqrt{1 + \frac{C_{\ell_1}^{\rm clust}}{C_{\ell_1}^{\rm white}}}\sqrt{1 + \frac{C_{\ell_2}^{\rm clust}}{C_{\ell_2}^{\rm white}}}\sqrt{1 + \frac{C_{\ell_3}^{\rm clust}}{C_{\ell_3}^{\rm white}}} \times\ b^{\rm white}_{\ell_1\ell_2\ell_3} \\ &= \alpha\sqrt{C_{\ell_1}^{\rm tot}\, C_{\ell_2}^{\rm tot}\, C_{\ell_3}^{\rm tot}}, \end{aligned} \tag{25}$$

with $b^{\rm white}_{\ell_1\ell_2\ell_3} = {\rm const}$ and $\alpha = \frac{b^{\rm white}_{\ell_1\ell_2\ell_3}}{\sqrt{C_{\ell_1}^{\rm white} C_{\ell_2}^{\rm white} C_{\ell_3}^{\rm white}}}$.

Equation (25) of the bispectrum relates to the clustered power spectrum or conversely the correlation function entering in the prescription.

### 3.3 Two populations of sources with clustering

The previous prescription, equation (24), describes well a single-point-source population. However, it fails at describing the cases where more than one population contribute to the signal. In particular, the case of the present generation of CMB experiments observing the CMB from low (30 GHz) to high (860 GHz) frequencies calls for an appropriate prescription which deals with independent source populations. Indeed, early results from the *Planck* mission (Planck Collaboration 2011b,c) show that radio and IR galaxies both contribute at frequencies of 100 GHz and above. In the following we thus extend and generalize the prescription accordingly.

Hence we define the harmonic coefficients as

$$a_{\ell m}^{\rm (tot)} = a_{\ell m}^{\rm (white,1)} + \sqrt{\frac{C_\ell^{\rm clust} + C_\ell^{\rm shot}}{C_\ell^{\rm white,2}}} \times a_{\ell m}^{\rm (white,2)}, \tag{26}$$

where $a_{\ell m}^{\rm (white,1)}$ and $a_{\ell m}^{\rm (white,2)}$ are independent realizations of white noise with different number counts. Index 1 refers to the radio population and 2 to the infrared population. The spectrum has then a form similar to the case of a single-source population:

$$C_\ell = C_\ell^{\rm clust} + C_\ell^{\rm shot,1+2}.$$

But the angular bispectrum differs and reads

$$b^{\rm tot}_{\ell_1\ell_2\ell_3} = b^{\rm white,1}_{\ell_1\ell_2\ell_3} + \sqrt{\frac{C_{\ell_1}^{\rm tot,2}}{C_{\ell_1}^{\rm white,2}}\frac{C_{\ell_2}^{\rm tot,2}}{C_{\ell_2}^{\rm white,2}}\frac{C_{\ell_3}^{\rm tot,2}}{C_{\ell_3}^{\rm white,2}}} \times b^{\rm white,2}_{\ell_1\ell_2\ell_3}. \tag{27}$$

For illustration, let us compare equations (25) and (27) in the equilateral configuration with white noises of both populations derived from the same number counts, and neglecting the shot noise of the second population:

$$b^{\rm 1pop}_{\ell\ell\ell} = \left(1 + \frac{C_\ell^{\rm clust}}{C_\ell^{\rm white}}\right)^{3/2} b^{\rm white}_{\ell\ell\ell}, \tag{28}$$

$$b^{\rm 2pop}_{\ell\ell\ell} = \left(1 + \left(\frac{C_\ell^{\rm clust}}{C_\ell^{\rm white}}\right)^{3/2}\right) b^{\rm white}_{\ell\ell\ell}. \tag{29}$$

The difference between these two formula is maximal when $C_\ell^{\rm clust}/C_\ell^{\rm white} \simeq 1$ and can be up to 40 per cent, illustrating the need to properly account for the different populations.

The two-population case, representative of the CMB context in the frequency range of interest, can be straightforwardly generalized to more point-source populations with or without clustering properties.

## 4 RESULTS

In this section we present the bispectra of radio and IR sources computed on simulations described below, showing the configuration dependence of the angular bispectrum and its frequency behaviour.

### 4.1 Data used

For our analysis, we used the all-sky simulated maps[3] of the IR and radio point sources provided by Sehgal et al. (2010) at 30, 90, 148, 219 and 350 GHz. We provide here a brief summary of the map construction. For a detailed description, we refer the reader to the above-cited paper. The maps are based on $N$-body simulations of the large-scale structure, with a volume 1000 $h^{-1}$ Mpc on a side, produced using a tree-particle mesh code. DM haloes are identified and are then populated with infrared and radio galaxies. The model for the radio sources is adapted so that the radio luminosity function matches that of the observed radio sources at 151 MHz.

The IR source model was partially based on Righi, Hernández-Monteagudo & Sunyaev (2008). The DM haloes are populated with galaxies of given luminosities taking into account a Poisson term and a correlation term. The model was constructed so that it is compatible with constraints on the luminosity function, the source counts and the fluctuations from Submillimetre Common-User Bolometer Array (SCUBA), Balloon-borne Large-Aperture Sub-millimeter Telescope (BLAST), *Spitzer* and Arcminute Cosmology Bolometer Array Receiver (ACBAR) (see Sehgal et al. 2010 for details). However, the simulation of IR sources, used here, does not account for the most recent observational constraints from ACT, SPT, *Herschel* and *Planck* results.

Maps of the different astrophysical contributions, in HEALPIX format at Nside = 8192, were produced by replication of one simulated octant of the sky. This procedure does not properly account for the signal at the largest scales especially up to the octopole, $\ell = 3$; it also introduces excess power at $\ell \leq 300$ for infrared sources as discussed by Sehgal et al. (2010), but the power is correct for higher multipoles. The produced maps have half-arcminute resolution but we degraded them to Nside = 1024 and used a uniform binning $\Delta\ell = 64$ to speed up computations. We checked that this procedure does not introduce a bias by comparing the binned spectrum in the degraded map to the unbinned spectrum in the original map and find excellent agreement. The octant replication in the map making translates mainly into a lack of power in the first bin (centred around $\ell = 32$) which is hence discarded in later plots.

### 4.2 Radio source characterization

We first investigate the bispectrum dependence on the configurations at a given frequency. We plot the angular bispectrum in four

[3] The frequency maps are available on Lambda website, http://lambda.gsfc.nasa.gov/toolbox/tb_cmbsim_ov.cfm

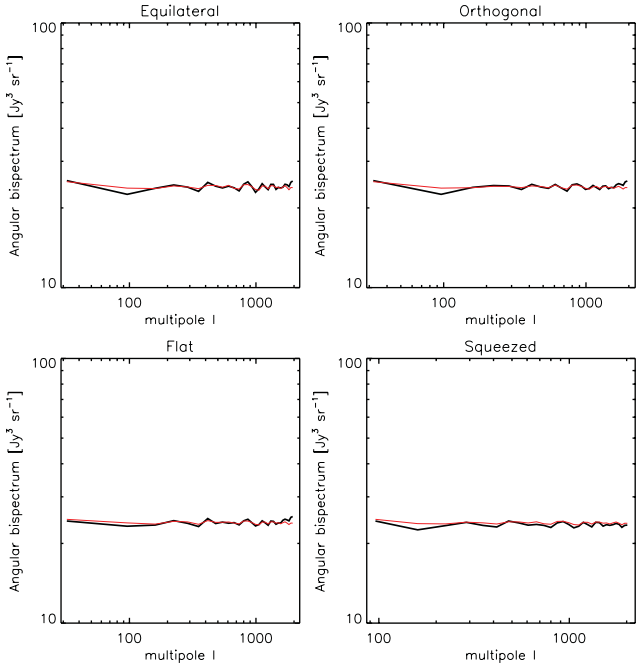


**Figure 3.** Thick black line: radio angular bispectrum at 90 GHz in different configurations: equilateral $(\ell, \ell, \ell)$, isosceles orthogonal $(\ell, \ell, \sqrt{2}\ell)$, isosceles flat $(\ell, \ell, 2\ell)$ and squeezed $(\ell_{\rm min}, \ell, \ell)$. The thin red line is the fit with prescription. The unit of the bispectra is $\mathrm{Jy}^3\ \mathrm{sr}^{-1}$.

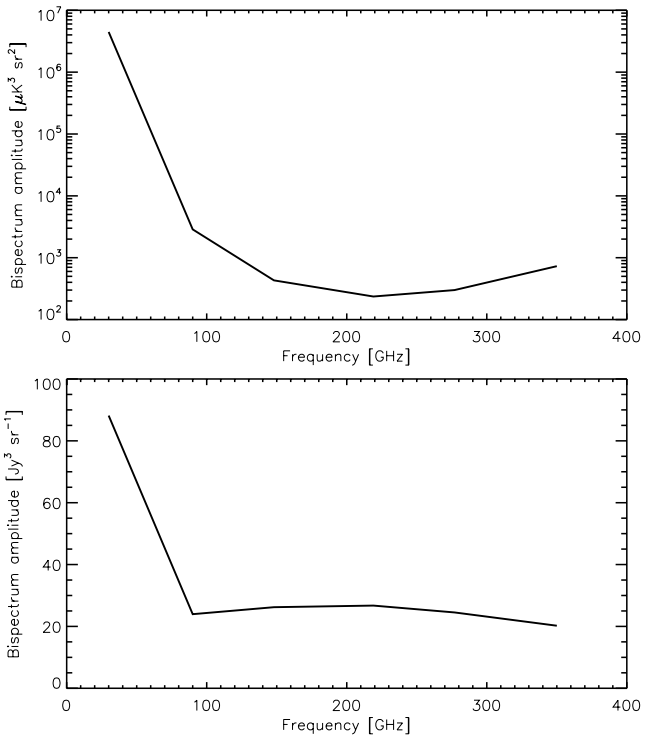


**Figure 4.** Amplitude of the radio angular bispectrum, averaged over all configurations, at 30, 219, 148, 277, 90 and 350 GHz, in temperature units for the upper panel and flux units for the bottom panel.

commonly used configurations, namely equilateral $(\ell, \ell, \ell)$, isosceles orthogonal $(\ell, \ell, \sqrt{2}\ell)$, isosceles flat $(\ell, \ell, 2\ell)$ and squeezed $(\ell_{\rm min}, \ell, \ell)$ configurations. They furthermore sample rather well the configuration space (see Fig. 1).

We see in Fig. 3, black thick line, that the bispectrum is constant. This result is independent of the frequency. Moreover, the value of the constant is independent of the configuration. This is what we expect from white noise and it shows that radio sources are indeed randomly distributed over the sky.

We show in Fig. 4 the dependence with frequency of the bispectrum amplitude averaged over all the configurations, in equivalent temperature unit for the upper panel and flux unit for the bottom panel. The amplitude is maximal at the lowest frequency 30 GHz; it then decreases to become mostly flat above 90 GHz because of free–free emission and inverted spectra sources.

The bispectrum was fitted with the one-population prescription described in Section 3.2, using the power spectrum extracted from the simulations and the multiplicative constant which minimizes the $\chi^2$ of the observed bispectrum to the prescribed one with error bars from Wick's expansion (see Appendix B). The fit of the bispectrum with the prescription is very good: Fig. 5 shows that the relative error (exact to fit) lies in the range between $-2$ per cent and $+2$ per cent with a mean relative error always less than 1.

### 4.3 IR source characterization

Fig. 6 shows the amplitude of the angular bispectrum in the equilateral configuration for the different frequencies. Dusty galaxy emission peaks at IR frequencies and plummets in the radio domain and so does the amplitude of the bispectrum. The bispectrum decreases with $\ell$, well fitted by a power law for $100 \leq \ell \leq 1000$, and with a flattening at higher multipoles. The decrease is expected from the clustering of IR galaxies on large scales. We found that the slopes were about the same for equilateral, flat and orthogonal configurations except for the squeezed triangles. Indeed, for the latter $\ell_1$ is fixed, while for the other configurations $\ell_1$, $\ell_2$, $\ell_3$ are all proportional to $\ell$.

The flattening of the bispectrum at high multipoles, indicative of the shot-noise contribution, occurs at lower multipoles with increasing frequency (e.g. at 350 GHz the bispectrum deviates from a power law at $\ell \sim 1000$ while at 90 GHz it is not before $\ell \sim 1500$). This is explained by the contribution of the high-flux galaxies, in Sehgal et al.'s simulations, that accounts for the shot noise ($b^{\rm shot} \sim \int S^3 \frac{{\rm d}n}{{\rm d}S} {\rm d}S$) and at the same time have a steeper emission than the galaxies accounting for the clustering term.

The bispectrum was fitted with the one-population prescription described in Section 3.2, using the multiplicative constant which minimizes the $\chi^2$, as previously for radio sources. We show in Fig. 7 how the bispectrum of the IR sources compares with the prescribed one. We see that the bispectrum obtained with the prescription is good, with a mean relative error always $\leq$5 per cent and a standard deviation $\leq$31 per cent. At 350 GHz an outlier at $-400\sigma$ was discarded for the computation of the standard deviation. Figs 5 and 7 show the distribution of the relative error between the bispectrum derived from the prescription and the actual bispectrum measured in the simulated maps. In other words, it exhibits departures from the predicted bispectrum values. The dispersion of these relative errors is larger for the IR sources (Fig. 7) than for the radio sources (Fig. 5) at all the frequencies. This behaviour is not an indication of a mismatch between the predicted and the actual bispectra; it relates to the intrinsic sample variance of both the IR and radio bispectra. The IR sources being weakly non-Gaussian (the value for $\alpha$ defined in equation (25) is $3 \times 10^{-3}$ for the IR sources, compared to 0.3 for radio sources) the variance of their bispectrum is indeed large compared to the bispectrum value (see Appendix B).

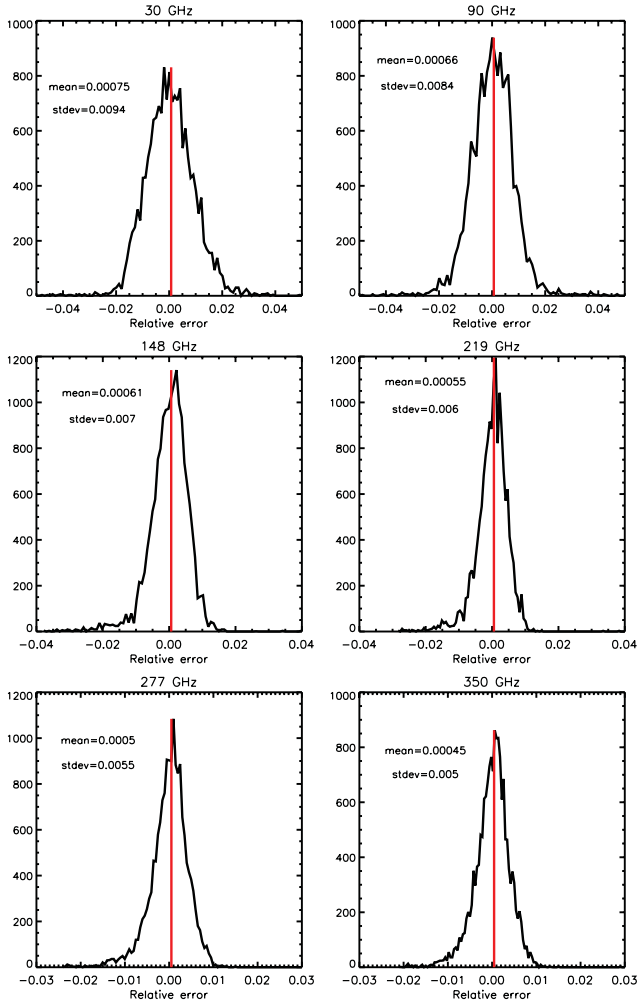


**Figure 5.** Relative error distribution with the prescription for radio sources alone. The vertical bar shows the mean of the distribution.

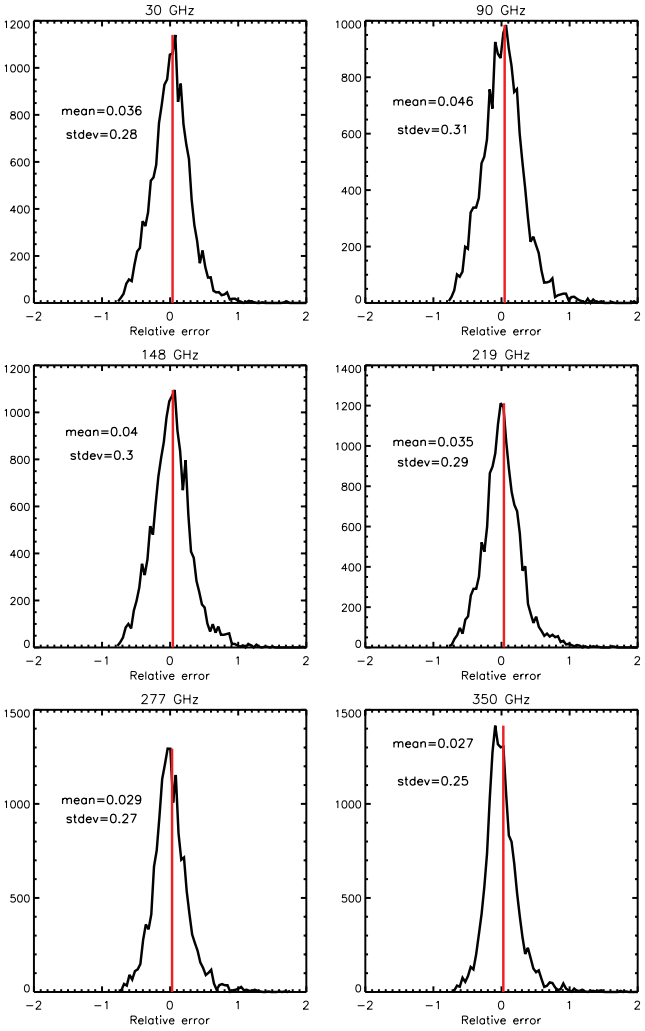


**Figure 7.** Relative error distribution with the prescription for infrared sources alone. The vertical bar shows the mean of the distribution. The quoted standard deviation at 350 GHz is computed after discarding one unique negative bispectrum outlier at $400\sigma$.

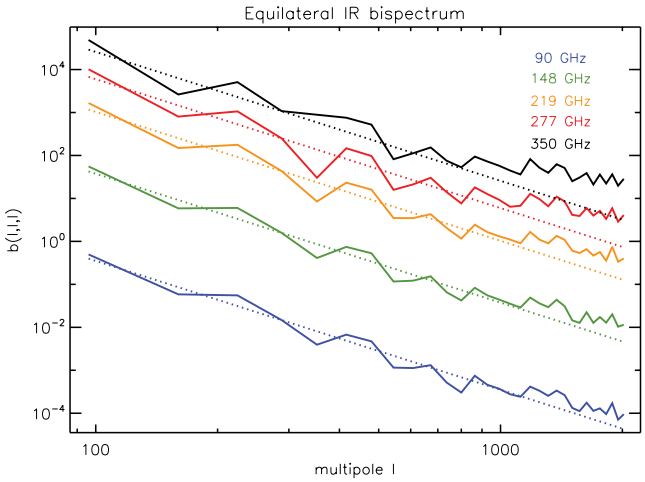


**Figure 6.** Infrared equilateral bispectrum at 90, 148, 219, 277 and 350 GHz from bottom to top. The dotted corresponding lines are the power-law fit.

### 4.4 Total contribution from IR and radio source populations

We now present the results when the two populations of sources contribute to the signal at the frequencies 30, 90, 148, 219, 277 and 350 GHz. To do so, we simply add the simulated maps at each frequency.

We illustrate the angular bispectrum dependence on frequency for one single configuration, namely equilateral, see Fig. 8.

The frequency behaviour is as expected from an independent combination of the IR and RAD bispectra. The radio source contribution dominates at low frequencies 30 and 90 GHz (blue and purple lines) and its bispectrum is flat. Infrared galaxies dominate at the highest frequencies 277 and 350 GHz (black and red upper lines) and show the characteristic power-law dependence due to clustering followed by the flattening of the bispectrum. At intermediate frequencies both populations contribute to the signal. The clustering-induced term of IR galaxies dominates on large angular scale while the random-noise term of radio galaxies dominates at small angular scale. The cross-over between radio and IR-galaxy bispectra is shifted to higher $\ell$s with increasing frequency. It is worth noting in Fig. 9 that at the lowest multipoles and at highest

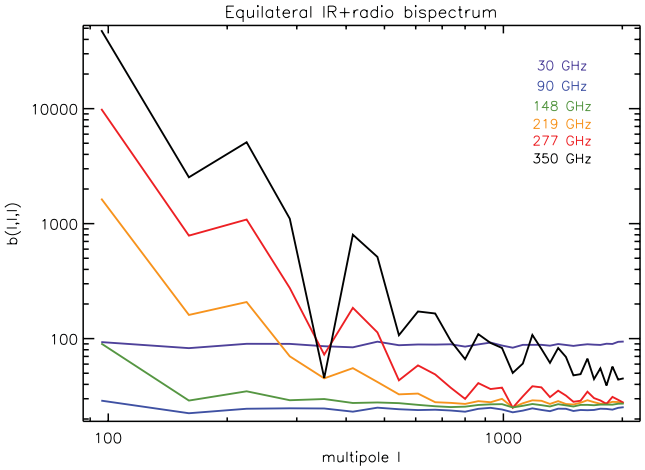


**Figure 8.** Infrared + radio orthogonal bispectrum at 30, 90, 148, 219, 277 and 350 GHz. The purple flat upper line is 30 GHz, the blue flat lowest line is 90 GHz and the more variable decreasing lines from bottom to top are 148, 219, 277 and 350 GHz.

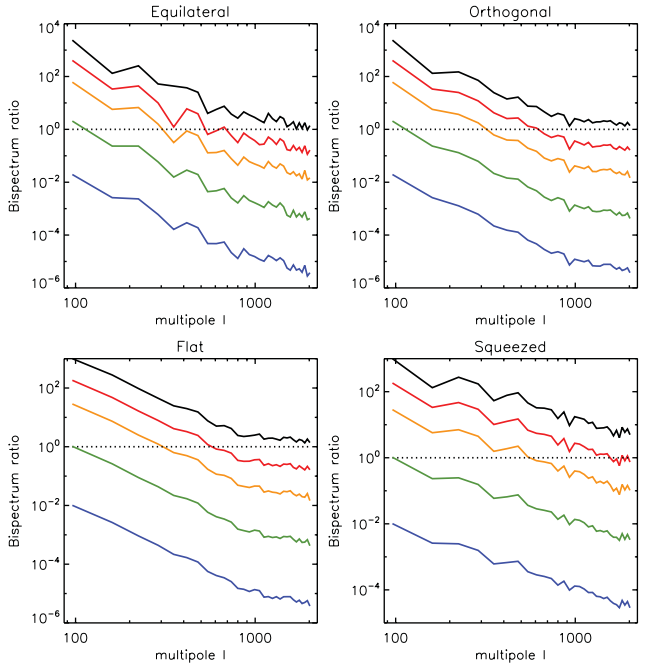


**Figure 9.** Ratio of the IR angular bispectrum to the radio one at 90, 148, 219, 277 and 350 GHz from bottom to top. The dotted line indicates equality.

frequencies, the IR galaxies produce a bispectrum at least 10 times more important than the radio sources.

We illustrate the angular bispectrum dependence on configurations at 350 GHz, see Fig. 10, thick black line. The error bars were computed in the weak NG approximation (see Appendix B). We note that infrared-radio cross-over occurs at about the same scale for the equilateral, orthogonal and flat configurations, but is at higher $\ell$ in squeezed configuration. This is expected because the squeezed IR bispectrum decreases more slowly than other configurations, one of the multipoles being fixed. Fig. 10 also displays

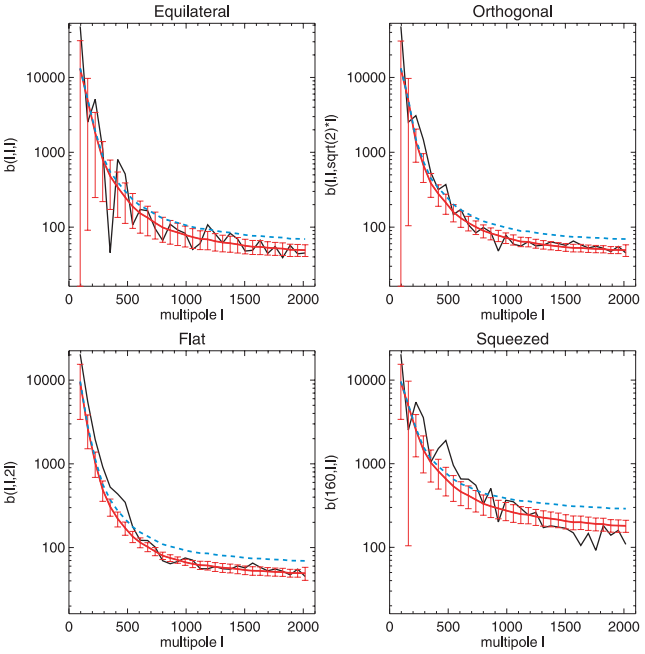


**Figure 10.** Infrared + radio bispectrum at 350 GHz in different configurations, with error bars. The thick black line is the computed bispectrum. The smoother solid lines are the fit with prescriptions: the upper blue line with the single-source prescription and the lower red line with the two-source prescription.

(thin red line) the bispectrum computed with two-population prescription derived in Section 3, i.e. adding up independently the prescription for radio sources and infrared sources derived in the previous sections. This is compared to a bispectrum computation considering only a single population (thin blue line). From Fig. 10, and Fig. 11 showing the distribution of relative errors with respect to these two prescriptions, we see that the two-population prescription performs much better than the single-population prescription. The former captures well the overall shape of the bispectrum and it adjusts particularly well the high $\ell$s. As a matter of fact, the mean relative error is lower than 2.5 per cent up to 350 GHz and the dispersion increases from 1 per cent at 30 GHz to 21 per cent at 350 GHz.

As expected, at 30 and 90 GHz the two prescriptions give same results since radio sources totally dominate the signal. At higher frequencies, both the mean errors and the dispersions derived using the two-population prescription are smaller than those obtained with the single-population prescription. Interestingly enough, at the highest frequency (350 GHz) where IR emission from galaxies is dominant, the single-population prescription is not satisfactory. As a matter of fact, configurations with at least one high multipole dominate the distributions (e.g. 7/8th of the configurations have at least one $\ell_i \geq 1000$). At 350 GHz these $\ell$s are dominated by infrared shot noise, so the computation of the prescriptions combine the IR shot noise and radio spectrum which are both flat. The radio emission is subdominant compared to infrared shot noise but nevertheless not negligible so the single-population prescription leads to an overestimate of the total bispectrum. This is clearly visible in Fig. 10 where the single-population prescription (blue thin line) is systematically higher than the computed bispectrum (black thick line) and the two-population prescription (red thin line), particularly at high multipoles.

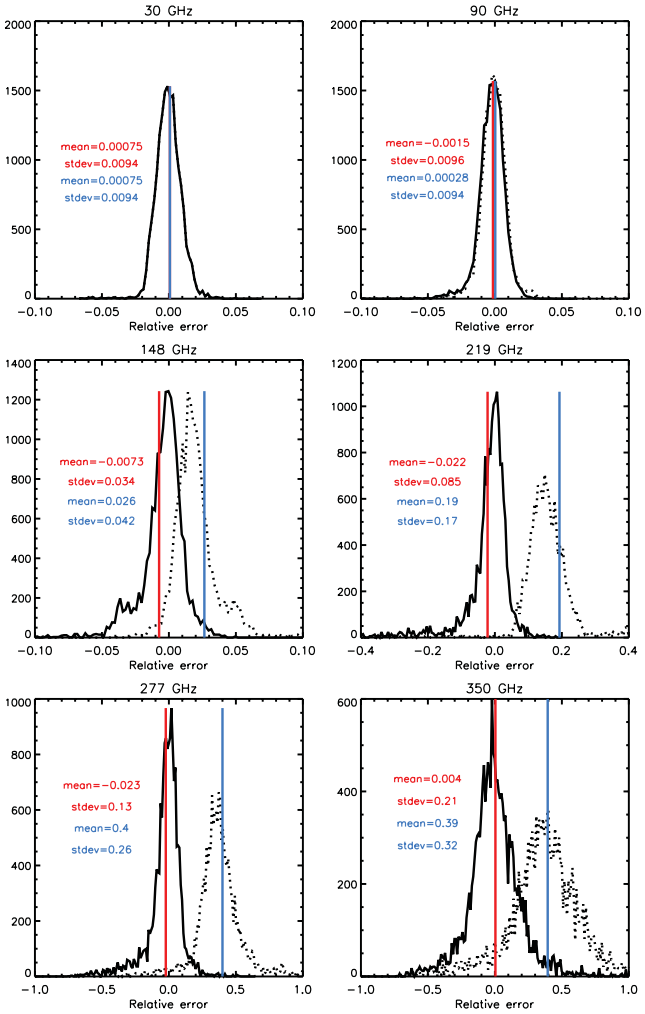


**Figure 11.** Relative error distribution with the prescriptions for the combination of infrared and radio sources. The dotted line is obtained with the single-population prescription, and the solid line with the two-populations prescription. The vertical bars show the mean of the distribution, the blue for the single-population prescription and the red for the two-population prescription.

## 5 CONSEQUENCES ON NON-GAUSSIANITY MEASURES

### 5.1 (*P*, *F*, *S*) parametrization

The parametrization of the angular bispectrum proposed in Section 2.3 allows us to visualize the bispectrum dependence on the configurations. The bispectrum is computed for 32 perimeters in the $\ell$ space. Only nine perimeters are shown for illustration in Figs 12 and 13, for the radio and IR-source populations, respectively. The bispectrum values are colour coded from blue (lowest value) to red (highest value). The succession of plots, arranged by increasing perimeters, exhibits the allowed configurations at given perimeter with the equilateral configuration being the starting (upper-left panel) and ending point (lower-right panel). Unsurprisingly, the bispectrum amplitude of the radio sources does not vary with the configuration (same colour code for all points in Fig. 12). As for the IR sources, Fig. 13, the bispectrum amplitude decreases with perimeter, thus from the upper-left to the lower-right panel. Moreover, it is worth noting that the bispectrum values do not vary vertically.

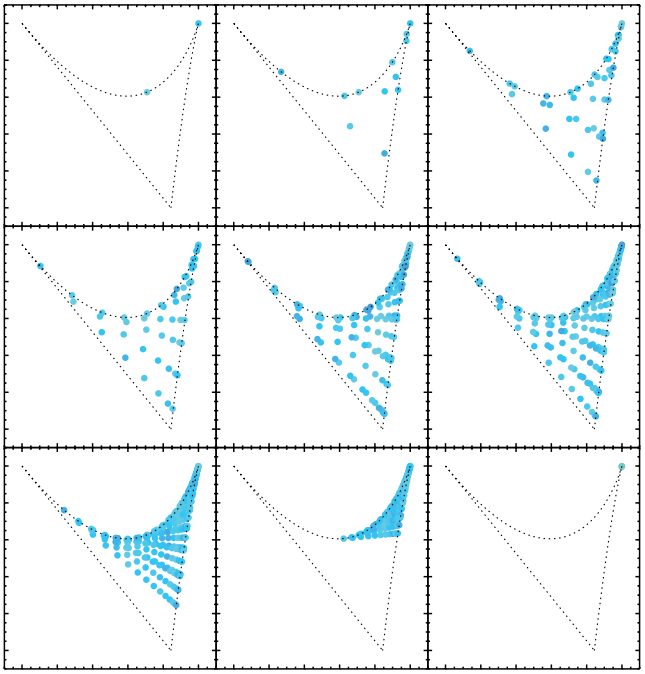

**Figure 12.** Radio bispectrum in the (*P*, *F*, *S*) parametrization at 90 GHz. Each plot is a slice of constant perimeter *P*; the value of the bispectrum is encoded in a logarithmic colour scale from violet-blue to red. The axes are the same as those in Fig. 1.

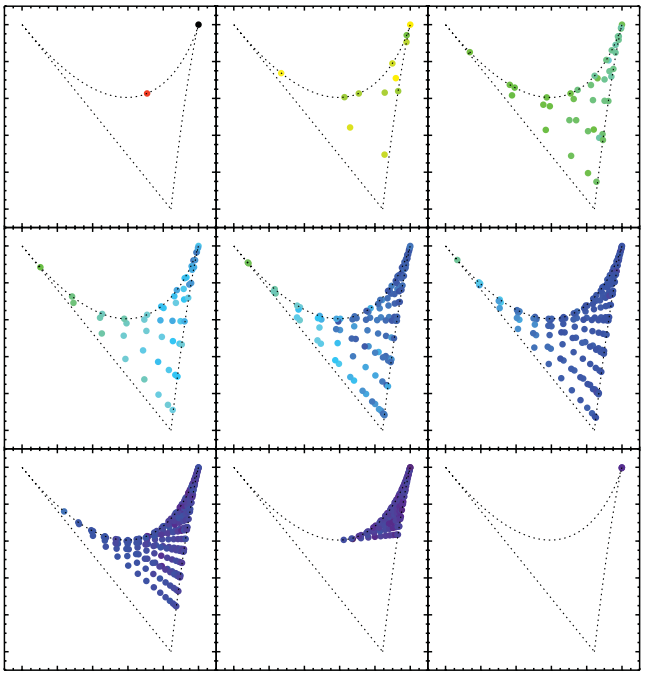

**Figure 13.** IR bispectrum in the (*P*, *F*, *S*) parametrization at 148 GHz. The axes are the same as those in Fig. 1.

This means that within the proposed (*P*, *F*, *S*) parametrization the bispectrum of the IR sources is quasi-independent of *F*, reducing the full bispectrum to a function of the two parameters *P* and *S*. Finally, at a given perimeter, i.e. scale, the bispectrum of the IR sources is more dependent on the configuration and peaks in the squeezed triangles, upper-left points in panels 2–5.

### 5.2 Point-source contamination of $f_{\rm NL}$

We now explore the point-source NG in terms of the contamination of the $f_{\rm NL}$ estimation. For pedagogical purposes, we consider the SW regime, i.e. a constant transfer function without acoustic oscillations, damping, etc.

For IR sources alone, which dominate at high frequencies, $b(\ell_1, \ell_2, \ell_3) \propto \sqrt{C_{\ell_1} C_{\ell_2} C_{\ell_3}}$. Combined with *Planck*'s latest constraints on the CIB $\ell \times C_\ell \simeq$ const (Planck Collaboration 2011d), this yields

$$b^{\rm IR}(\ell_1, \ell_2, \ell_3) \propto \frac{1}{\sqrt{\ell_1 \ell_2 \ell_3}},$$

which has a similar shape to the local template in the SW limit, equation (13). We define the scalar product between the bispectra $f, g$:

$$\langle f, g \rangle = \sum_{\ell_1 \le \ell_2 \le \ell_3} N_{\ell_1 \ell_2 \ell_3} \frac{f(\ell_1, \ell_2, \ell_3) \times g(\ell_1, \ell_2, \ell_3)}{C^{\rm CMB}_{\ell_1} C^{\rm CMB}_{\ell_2} C^{\rm CMB}_{\ell_3}},$$

where the denominator is the variance of the local bispectrum, for triangles with $\ell_1 \neq \ell_2 \neq \ell_3$. The correlation coefficient between a bispectrum $b^\alpha$ and the local bispectrum $b^{\rm loc}$ is

$$\cos\theta_\alpha = \frac{\langle b^\alpha, b^{\rm loc} \rangle}{\|b^\alpha\| \, \|b^{\rm loc}\|},$$

with $\alpha$ being IR or radio.

Fig. 14 shows that, for $\ell < 200$, the correlation between radio and local bispectra decreases quickly, so that the two bispectra may be distinguished efficiently. Conversely, even when using a large multipole range, the IR bispectrum is significantly correlated with the local one.

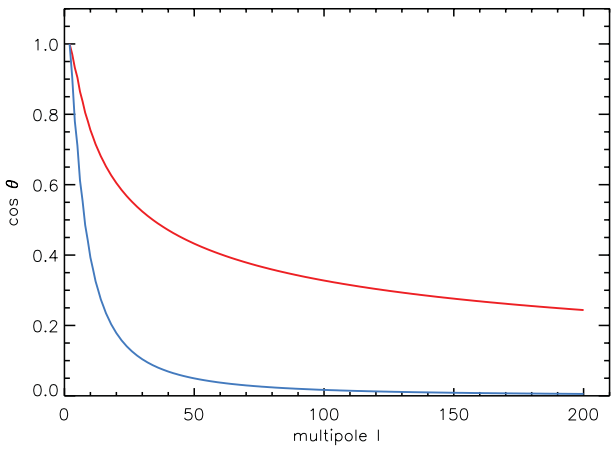


**Figure 14.** Correlation between SW local bispectrum and, respectively, IR (red) and radio (blue) bispectrum, as a function of the maximum multipole used ($\ell_{\rm min} = 2$).

The contribution of the bispectrum of a point-source population $\alpha$ to $f_{\rm NL}$ is

$$\Delta f^\alpha_{\rm NL} = \frac{\langle b^\alpha, b^{f_{\rm NL}=1} \rangle}{\langle b^{f_{\rm NL}=1}, b^{f_{\rm NL}=1} \rangle} = \frac{\|b^\alpha\|}{\|b^{f_{\rm NL}=1}\|} \cos\theta_\alpha. \quad (30)$$

This equation is the usual bias (Serra & Cooray 2008) of the local-optimized NG estimator, when the local bispectrum has the form of equation (13).

A more comprehensive computation of $\Delta f^\alpha_{\rm NL}$ is achievable by applying the full local estimator described in Section 2.2. We built up this estimator using the full transfer function from the latest version of CAMB (Lewis et al. 2000) with WMAP7+BAO+H0 cosmological parameters (Larson et al. 2011), and we tested the estimator on simulations from Elsner & Wandelt (2009). We found the previously noted result that the variance of the estimator increases with $f_{\rm NL}$. It is unbiased in the range we have tested ($0 \le f_{\rm NL} \le 200$).

We used this $f_{\rm NL}$ estimator on two sets of simulated maps: maps containing all the point sources and maps with only sources below the flux limit of Planck's Early Release Compact Source Catalogue (ERCSC) (Planck Collaboration 2011a), namely $S_{\rm c}$ =0.5, 0.5, 0.3, 0.3, 0.3 and 0.25 Jy as a function of frequency. Moreover, we have computed the estimator at three resolutions, $\ell_{\rm max}$, recalibrating the $S_{\rm prim}$ normalization in each case. Tables 1 and 2 summarize these results.

The bias $\Delta f^{\rm RAD}_{\rm NL}$ (see Table 1) is negative on large angular scales, for $\ell_{\rm max} = 50$. The bias due to radio sources becomes positive at higher multipoles in agreement with Serra & Cooray (2008). This is due to the CMB bispectrum being negative in the SW-dominated regime and the radio bispectrum being positive. The bias increases by five orders of magnitude at the highest resolution, $\ell_{\rm max} = 2048$. The reason for the rapid increase of the bias with $\ell_{\rm max}$ relates to the weight of the observed bispectrum in equation (17), $B^{\rm loc}_{\ell_1 \ell_2 \ell_3} / C_{\ell_1} C_{\ell_2} C_{\ell_3}$, which rapidly increases with multipole as the product of spectra decreases more quickly than the bispectrum. This leads to a $1/C_\ell$ dependence in squeezed configurations and to a $1/C^2_\ell$ dependence in equilateral configurations. When the observed bispectrum is associated with a CMB signal alone, its decrease cancels the increase of the weights so that the sum in equation (17) converges. Conversely, the sum diverges when the observed bispectrum is associated with a non-CMB signal and does not decrease with $\ell$ as fast as the CMB.

The bias $\Delta f^{\rm RAD}_{\rm NL}$ is maximal at 30 GHz and rapidly decreases with frequency. It slightly increases again at the two highest frequencies following the amplitude of the bispectrum in temperature units which is plotted in the upper panel of Fig. 4. The relative error of $\Delta f^{\rm RAD}_{\rm NL}$ for $\ell_{\rm max} = 700$ is of the order of 1.5 per cent independently of the frequency. It amounts to 2.3 per cent for $\ell_{\rm max} = 2048$. These

**Table 1.** Bias on the $f_{\rm NL}$ estimator, $\Delta f^{\rm RAD}_{\rm NL}$, due to radio sources.

| $\nu$ (GHz) | 30 | 90 | 148 | 219 | 277 | 350 |
|---|---|---|---|---|---|---|
| | | | without flux cut | | | |
| $\ell_{\rm max} = 50$ | −4.2 | −0.0025 | −0.000 37 | −0.000 21 | −0.000 27 | −0.000 68 |
| $\ell_{\rm max} = 700$ | 3850 | 2.5 | 0.38 | 0.21 | 0.27 | 0.65 |
| $\ell_{\rm max} = 2048$ | 177 000 | 117 | 18 | 9.7 | 12 | 30 |
| | | | with flux cut | | | |
| $\ell_{\rm max} = 700$ | 108 | 0.17 | 0.0071 | 0.0031 | 0.0035 | 0.0064 |
| $\ell_{\rm max} = 2048$ | 4930 | 7.5 | 0.31 | 0.14 | 0.16 | 0.29 |

**Table 2.** Bias of the $f_{\rm NL}$ estimator, $\Delta f_{\rm NL}^{\rm IR}$, due to IR sources.

| $\nu$ (GHz) | 30 | 90 | 148 | 219 | 277 | 350 |
|---|---|---|---|---|---|---|
| | | | without flux cut | | | |
| $\ell_{\rm max} = 50$ | $-3.5 \times 10^{-8}$ | $-5.9 \times 10^{-6}$ | $-9.2 \times 10^{-5}$ | $-0.0027$ | $-0.023$ | $-1.0$ |
| $\ell_{\rm max} = 700$ | $-1.3 \times 10^{-6}$ | $-0.000\,19$ | $-0.0033$ | $-0.063$ | $-0.55$ | $-9.0$ |
| $\ell_{\rm max} = 2048$ | $-1.8 \times 10^{-5}$ | $-0.0026$ | $-0.039$ | $-0.68$ | $-4.8$ | $-67$ |
| | | | with flux cut | | | |
| $\ell_{\rm max} = 700$ | $-1.3 \times 10^{-6}$ | $-0.000\,19$ | $-0.0033$ | $-0.078$ | $-0.74$ | $-11$ |
| $\ell_{\rm max} = 2048$ | $-1.8 \times 10^{-5}$ | $-0.0026$ | $-0.039$ | $-0.67$ | $-6.3$ | $-66$ |

error bars were computed with simulations using the catalogue of sources present in Sehgal et al.'s maps.

As shown in Table 1, masking sources above the ERCSC flux limit proves very efficient to significantly decrease the radio contamination to $f_{\rm NL}$ at all the frequencies. At a *Planck*-like resolution, $\ell_{\rm max} = 2048$, the bias $\Delta f_{\rm NL}^{\rm RAD}$ is reduced below unity above 150 GHz. It is of the order of *Planck*'s expected error bars at 90 GHz. At 30 GHz the bias is still important.

The bias due to IR sources $\Delta f_{\rm NL}^{\rm IR}$ is always negative, see Table 2. As a matter of fact, we have shown that the IR bispectrum peaks in squeezed configurations just like the CMB bispectrum and these configurations thus dominate the sum in equation (17). Moreover, in the squeezed limit the CMB bispectrum is negative while the IR bispectrum is positive. For the same reason as for radio sources, the bias $\Delta f_{\rm NL}^{\rm IR}$ blows up at high multipoles. This is particularly important at a *Planck*-like resolution, $\ell_{\rm max} = 2048$, where primordial NG tests will need to carefully handle the contamination by IR sources. The IR source emission plummets at radio frequencies so that $\Delta f_{\rm NL}^{\rm IR}$ is completely negligible below 220 GHz. It becomes of the order of *Planck*'s error bars at 277 GHz and it reaches *WMAP*'s central values for $f_{\rm NL}$ at 350 GHz. The relative error of $\Delta f_{\rm NL}^{\rm IR}$ ranges between 6 and 7 per cent from 148 to 350 GHz for $\ell_{\rm max} = 700$. It ranges between 3 and 7 per cent for $\ell_{\rm max} = 2048$. (These error bars were computed analytically with the weak NG approximation – see Appendix B.) At higher frequencies the IR contamination to the bispectrum is likely larger but the contamination from our Galaxy needs to be taken into account as well.

Interestingly, masking sources above the ERCSC flux limit does not diminish $\Delta f_{\rm NL}^{\rm IR}$, as most of the IR sources are unresolved and the IR clustering is mostly due to faint sources. Masking may even artificially boost $\Delta f_{\rm NL}^{\rm IR}$, for example at 277 GHz, since it mostly affects the flat shot noise which produces a positive bias $\Delta f_{\rm NL}$.

## 6 CONCLUSIONS AND DISCUSSION

We have studied the NG produced by point sources in the frequency range of the CMB from 30 to 350 GHz. We have developed a simple and accurate prescription to infer the angular bispectrum from the power spectrum of point sources, considering different independent populations of sources, with or without clustering.

Using publicly available all-sky simulations of radio and IR sources, we have computed the full-sky binned bispectra for these two populations of sources. We have compared the measured bispectra to those predicted from our prescription and found very good agreement between the two. We have displayed the angular bispectrum using a new parametrization which highlights efficiently the configuration dependence.

We have characterized the angular bispectrum of the IR and radio sources showing the configuration dependence and the frequency behaviour. In particular and for the first time, we showed that the IR bispectrum peaks in the squeezed triangles and that the clustering of IR sources enhances the bispectrum values by several orders of magnitude on large angular scales $\ell \sim 100$. The bispectrum of IR sources starts to dominate that of radio sources on large angular scales at 150 GHz, and it dominates the whole multipole range at 350 GHz.

Finally, to illustrate the contamination of local CMB NG by point sources, we derive the bias on $f_{\rm NL}$ induced by radio and IR sources, for *WMAP* or *Planck*-like angular resolutions. Radio sources produce a positive bias which is significantly reduced ($\Delta f_{\rm NL} < 1$ for $\nu \geq 150$ GHz) by masking the sources above a given flux limit taken as the ERCSC cut. The form of the IR bispectrum mimics a primordial 'local' bispectrum, $f_{\rm NL}$, on large angular scales. The IR sources produce a negative bias which becomes important for *Planck*-like resolution and at high frequencies ($\Delta f_{\rm NL} \sim -6$ at 277 GHz and $\Delta f_{\rm NL} \sim -60$–$70$ at 350 GHz). Most of the signal is associated with the clustering of faint IR sources. Therefore, the bias $\Delta f_{\rm NL}^{\rm IR}$ is not reduced by masking sources above a flux limit but, in some cases, even increased due to the reduction of the shot-noise term.

Our analysis highlights the sensitivity of the bias on $f_{\rm NL}$ to the experimental properties (maximum resolution and frequency range), the point-source models (clustering or no, resolved or not) and their scale dependence with respect to the CMB. For high-resolution, high-frequency CMB experiments, primordial NG estimations need to take special care of astrophysical contaminations. One solution would be to estimate the primordial and astrophysical NG simultaneously.

## ACKNOWLEDGMENTS

The authors thank an anonymous referee for comments and suggestions. They wish to thank S. Ilic, G. Lagache and A. Penin for useful discussions. They acknowledge the use of Lambda archive,[4] CAMB (Lewis et al. 2000) and the HEALPIX (Gorski et al. 2005) package. They made use of all-sky simulations of the microwave sky by Sehgal et al. (2010) and non-Gaussian CMB simulations by Elsner & Wandelt (2009). NA and FL thank Université de Genève and the Swiss NSF for partial support and hosting, and MK and MF thank the IAS for hospitality on numerous occasions. The authors acknowledge partial support from PHC Germaine de Staël. FL further acknowledges financial support from a PhD fellowship of the Ecole Normale Supérieure Paris. MK and MF acknowledge

[4] http://lambda.gsfc.nasa.gov/toolbox/tb_cmbsim_ov.cfm

funding by the Swiss NSF. Part of the calculations were performed on the *Andromeda* cluster of the Université de Genève.

## REFERENCES


Acquaviva V., Bartolo N., Matarrese S., Riotto A., 2003, Nuclear Phys. B, 667, 119
Aghanim N., Kunz M., Castro P., Forni O., 2003, A&A, 406, 797
Aghanim N., Majumdar S., Silk J., 2008, Rep. Progress Phys., 71, 066902
Amblard A. et al., 2011, Nat, 470, 510
Argueso F., GonzalezNuevo J., Toffolatti L., 2003, ApJ, 598, 86
Astier P. et al., 2006, A&A, 447, 31
Babich D., Pierpaoli E., 2008, Phys. Rev. D, 77, 123011
Barrientos L. F., Battistelli E. S., Bond J. R., Brown B., Burger B., Chervenak J., 2010, preprint (arXiv:1009.0847v1)
Bartolo N., Komatsu E., Matarrese S., Riotto A., 2004, Phys. Rep., 402, 103
Bassett B. A., Tsujikawa S., Wands D., 2006, Rev. Modern Phys., 78, 537
Blake C. et al., 2011, MNRAS, 415, 2892
Boughn S. P., Partridge R. B., 2008, PASP, 120, 281
Bucher M., Tent B. V., Carvalho C. S., 2010, MNRAS, 407, 2193
Byrnes C. T., Choi K.-Y., 2010, Advances Astron., 2010, 1
Cooray A., Kesden M., 2002, New Astron., 8, 21
Creminelli P., Zaldarriaga M., 2004, J. Cosmol. Astropart. Phys., 2004, 006
Creminelli P., Nicolis A., Senatore L., Tegmark M., Zaldarriaga M., 2006, J. Cosmol. Astropart. Phys., 2006, 004
De Troia G. et al., 2003, MNRAS, 343, 284
de Zotti G., Ricci R., Mesa D., Silva L., Mazzotta P., Toffolatti L., González-Nuevo J., 2005, A&A, 431, 893
Elsner F., Wandelt B. D., 2009, ApJS, 184, 264
Fergusson J. R., Liguori M., 2010, preprint (arXiv:1006.1642)
Freedman W. L. et al., 2001, ApJ, 553, 47
Freedman W. L. et al., 2009, ApJ, 704, 1036
González-Nuevo J., Toffolatti L., Argüeso F., 2005, ApJ, 621, 1
Gorski K. et al., 2005, ApJ, 622, 759
Guth A. H., 1981, Phys. Rev. D, 23, 347
Guy J. et al., 2010, A&A, 523, A7
Hall N. R. et al., 2010, ApJ, 718, 632
Hicken M., Wood-Vasey W. M., Blondin S., Challis P., Jha S., Kelly P. L., Rest A., Kirshner R. P., 2009, ApJ, 700, 1097
Keisler R. et al., 2011, ApJ, 743, 28
Komatsu E., Spergel D. N., 2001, Phys. Rev. D, 63, 063002
Komatsu E., Wandelt B. D., Spergel D. N., Banday A. J., Górski K. M., 2002, ApJ, 566, 19
Komatsu E., Spergel D. N., Wandelt B. D., 2005, ApJ, 634, 14
Komatsu E. et al., 2009, ApJS, 180, 330
Komatsu E. et al., 2011, ApJS, 192, 18
Kunz M., Banday A. J., Castro P. G., Ferreira P. G., Górski K. M., 2001, ApJ, 563, L99
Lagache G., Puget J. L., 2000, A&A, 355, 17
Lagache G., Bavouzet N., Fernandez-Conde N., Ponthieu N., Rodet T., Dole H., Miville-Deschênes M.-a., Puget J.-L., 2007, ApJ, 665, L89
Larson D. et al., 2011, ApJS, 192, 16
Lesgourgues J., 2011, preprint (arXiv:1104.2932)
Lewis A., 2011, J. Cosmol. Astropart. Phys., 10, 026
Lewis A., Challinor A., Lasenby A., 2000, ApJ, 538, 473
Liddle A. R., Lyth D. H., 2000, Cosmological Inflation and Large-Scale Structure. Cambridge University Press, Cambridge
Linde A., 2008, in Lemoine M., Martin J., Peter P., eds, Lecture Notes in Physics, Vol. 738, Inflationary Cosmology. Springer Verlag, Berlin, p. 1
Low F. J., Tucker W. H., 1968, Phys. Rev. Lett., 21, 1538
Maldacena J., 2003, J. High Energy Phys., 2003, 013
Matsuhara H. et al., 2000, A&A, 361, 407
Munshi D., Valageas P., Cooray A., Heavens A., 2009, MNRAS, 000, 1
Percival W. J. et al., 2010, MNRAS, 401, 2148
Planck Collaboration 2011a, A&A, 536, A7
Planck Collaboration 2011b, A&A, 536, A13
Planck Collaboration 2011c, A&A, 536, A15
Planck Collaboration 2011d, A&A, 536, A18
Planck Collaboration 2011e, A&A, 536, A24
Puget J.-L., Abergel A., Bernard J.-P., Boulanger F., Burton W. B., Desert F.-X., Hartmann D., 1996, A&A, 308, 5
Renaux-Petel S., 2009, J. Cosmol. Astropart. Phys., 10, 012
Riess A. G. et al., 2009, ApJ, 699, 539
Righi M., Hernández-Monteagudo C., Sunyaev R. A., 2008, A&A, 478, 685
Sachs R. K., Wolfe A. M., 1967, ApJ, 147, 73
Sajina A., Partridge B., Evans T., Stefl S., Vechik N., Myers S., Dicker S., Korngut P., 2011, ApJ, 732, 45
Sehgal N., Bode P., Das S., Hernandez-Monteagudo C., Huffenberger K., Lin Y.-T., Ostriker J. P., Trac H., 2010, ApJ, 709, 920
Seljak U., Zaldarriaga M., 1996, ApJ, 469, 437
Serra P., Cooray A., 2008, Phys. Rev. D, 77, 1
Smoot G. F. et al., 1992, ApJ, 396, L1
Spergel D., Goldberg D., 1999, Phys. Rev. D, 59, 1
Starobinskiĭ A. A., 1979, Soviet J. Exp. Theor. Phys. Lett., 30, 682
Sunyaev R. A., Zeldovich Y. B., 1972, Comments Astrophys. Space Phys., 4, 173
Toffolatti L., Argueso Gomez F., de Zotti G., Mazzei P., Franceschini A., Danese L., Burigana C., 1998, MNRAS, 297, 117
Viero M. P. et al., 2009, ApJ, 707, 1766
Wick G. C., 1950, Phys. Rev., 80, 268


## APPENDIX A: CLUSTERED SOURCES SHOT NOISE

A source with flux $S$ enclosed in a pixel $\Omega_{\rm pix}$ yields a rise of temperature compared to the CMB:

$$\Delta T = \frac{S}{\Omega_{\rm pix}} \times \underbrace{\frac{(\mathrm{e}^x-1)^2}{x^2\mathrm{e}^x} \times \frac{c^2}{2\nu^2 k_{\rm B}}}_{\equiv k_\nu}, \tag{A1}$$

where $x = h\nu/k_{\rm B}T_{\rm CMB}$ and $k_\nu = \left.\frac{\partial B(\nu,T)}{\partial T}\right|_{T_{\rm CMB}}$.

The two-point correlation function of point sources takes the form

$$\langle \Delta T(\boldsymbol{n}) \Delta T(\boldsymbol{n}')\rangle = F(\boldsymbol{n},\boldsymbol{n}') + \Gamma\,\delta_{\boldsymbol{n},\boldsymbol{n}'},$$

where $F(\boldsymbol{n},\boldsymbol{n}')$ is the correlation function coming from the spatial distribution of the sources, and the Kronecker term comes from the discreteness of the sources:

$$\Gamma = \langle \Delta T^2\rangle - F(\boldsymbol{n},\boldsymbol{n}).$$

Assuming statistical isotropy, we get

$$C_\ell = C_\ell^{\rm clust} + C_\ell^{\rm shot} \quad \text{with} \quad C_\ell^{\rm shot} = \Gamma\,\Omega_{\rm pix}.$$

Indeed,

$$\begin{aligned}
\langle a_{\ell m}\, a^*_{\ell' m'}\rangle &= \int \mathrm{d}^2\boldsymbol{n}\,\mathrm{d}^2\boldsymbol{n}'\, Y_{\ell m}(\boldsymbol{n})\, Y^*_{\ell' m'}(\boldsymbol{n}')\langle \Delta T(\boldsymbol{n})\Delta T(\boldsymbol{n}')\rangle \\
&= \underbrace{\int \mathrm{d}^2\boldsymbol{n}\,\mathrm{d}^2\boldsymbol{n}'\, Y_{\ell m}(\boldsymbol{n})\, Y^*_{\ell' m'}(\boldsymbol{n}')\, F(\boldsymbol{n},\boldsymbol{n}')}_{= C_\ell^{\rm clust}\,\delta_{\ell\ell'}\,\delta_{mm'}} \\
&\quad + \sum_{\boldsymbol{n}_i,\boldsymbol{n}'_j} Y_{\ell m}(\boldsymbol{n}_i)\, Y^*_{\ell' m'}(\boldsymbol{n}'_j) \times \Gamma\,\delta_{\boldsymbol{n}_i,\boldsymbol{n}'_j}\,\Omega^2_{\rm pix} \\
&= C_\ell^{\rm clust}\,\delta_{\ell\ell'}\,\delta_{mm'} + \Gamma\,\Omega_{\rm pix}\sum_{\boldsymbol{n}_i} Y_{\ell m}(\boldsymbol{n}_i)\, Y^*_{\ell' m'}(\boldsymbol{n}_i)\,\Omega_{\rm pix} \\
&= C_\ell^{\rm clust}\,\delta_{\ell\ell'}\,\delta_{mm'} + \Gamma\,\Omega_{\rm pix}\int \mathrm{d}^2\boldsymbol{n}\, Y_{\ell m}(\boldsymbol{n})\, Y^*_{\ell' m'}(\boldsymbol{n}) \\
&= C_\ell^{\rm clust}\,\delta_{\ell\ell'}\,\delta_{mm'} + \Gamma\,\Omega_{\rm pix}\,\delta_{\ell\ell'}\,\delta_{mm'}.
\end{aligned} \tag{A2}$$

$C_\ell$ has units $\mu\mathrm{K}^2$ sr. Let us number by $i = 1, \ldots, N$ all sources of the sky; then the temperature of a pixel is given by

$$\Delta T(\boldsymbol{n}) = \frac{k_\nu}{\Omega_{\rm pix}} \sum_{i=1}^{N} S_i \times \mathbb{1}_{[i\in\boldsymbol{n}]}, \tag{A3}$$

where $\mathbb{1}_{[i\in\boldsymbol{n}]}$ is 1 if the source $i$ is in the pixel and 0 otherwise. We have

$$\langle \mathbb{1}_{[i\in\boldsymbol{n}]}\rangle = 1/n_{\rm pix}.$$

Hence for $\boldsymbol{n}\neq\boldsymbol{n}'$,

$$F(\boldsymbol{n},\boldsymbol{n}') = \langle \Delta T(\boldsymbol{n})\Delta T(\boldsymbol{n}')\rangle = \frac{k_\nu^2}{\Omega_{\rm pix}^2}\left\langle \sum_{i\neq j} S_i\, S_j \times \mathbb{1}_{[i\in\boldsymbol{n}]}\mathbb{1}_{[j\in\boldsymbol{n}']}\right\rangle.$$

Then we find

$$\begin{aligned}\langle \Delta T(\boldsymbol{n})^2\rangle &= \frac{k_\nu^2}{\Omega_{\rm pix}^2}\left\langle \sum_{i,j=1}^{N} S_i\, S_j \times \mathbb{1}_{[i\in\boldsymbol{n}]}\mathbb{1}_{[j\in\boldsymbol{n}]}\right\rangle\\ &= \frac{k_\nu^2}{\Omega_{\rm pix}^2}\left\langle \sum_{i\neq j} S_i\, S_j \times \mathbb{1}_{[i\in\boldsymbol{n}]}\mathbb{1}_{[j\in\boldsymbol{n}]}\right\rangle\\ &\quad + \frac{k_\nu^2}{\Omega_{\rm pix}^2}\sum_{i=1}^{N} S_i^2 \times \langle \mathbb{1}_{[i\in\boldsymbol{n}]}\rangle\\ &= \lim_{\boldsymbol{n}\to\boldsymbol{n}'}\langle \Delta T(\boldsymbol{n})\Delta T(\boldsymbol{n}')\rangle + \frac{k_\nu^2}{\Omega_{\rm pix}^2}\frac{1}{n_{\rm pix}}\sum_{\rm sources} S^2.\end{aligned}$$

Recalling $\Omega_{\rm pix} = \frac{4\pi}{n_{\rm pix}}$ and introducing $\frac{{\rm d}n}{{\rm d}S}$ the number counts of sources

$$\langle \Delta T(\boldsymbol{n})^2\rangle = F(\boldsymbol{n},\boldsymbol{n}) + \underbrace{\frac{k_\nu^2}{4\pi\,\Omega_{\rm pix}}\int S^2\,\frac{{\rm d}n}{{\rm d}S}\,{\rm d}S}_{=\Gamma}.$$

And finally

$$C_\ell^{\rm shot} = \Gamma\,\Omega_{\rm pix} = \frac{k_\nu^2}{4\pi}\int S^2\,\frac{{\rm d}n}{{\rm d}S}\,{\rm d}S, \tag{A4}$$

which is the shot-noise formula (19).

The integrals run from $S=0$ to $S_{\rm cut}$, the flux detection limit of the survey, i.e. sources with $S>S_{\rm cut}$ have been removed. Note that this result is independent of the two-point correlation function, which we did not specify.

At order 3 for the angular bispectrum, the computation is a bit more involved but follows the same line, and we find

$$\langle a_{\ell_1 m_1} a_{\ell_2 m_2} a_{\ell_3 m_3}\rangle = G^{m_1 m_2 m_3}_{\ell_1\ell_2\ell_3}\times b_{\ell_1\ell_2\ell_3} \tag{A5}$$

with

$$b^{\rm shot}_{\ell_1\ell_2\ell_3} = \frac{k_\nu^3}{4\pi}\times\int S^3\,\frac{{\rm d}n}{{\rm d}S}\,{\rm d}S, \tag{A6}$$

which is the shot-noise formula (20).

## APPENDIX B: BISPECTRUM VARIANCE IN THE WEAK NG APPROXIMATION

The bispectrum estimator (4) can be put in the form

$$\hat{b}_{123} = \frac{1}{N_{123}}\times\sum_{m_{123}} G_{123}\, a_1\, a_2\, a_3, \tag{B1}$$

where a shortened notation is used: $N_{123}$ is the number of triangles defined in equation (6) and $G_{123}$ is the Gaunt coefficient:

$$G_{123} = \int {\rm d}^2\boldsymbol{n}\, Y_{\ell_1 m_1}(\boldsymbol{n}) Y_{\ell_2 m_2}(\boldsymbol{n}) Y_{\ell_3 m_3}(\boldsymbol{n}). \tag{B2}$$

Then the bispectrum covariance takes the form

$$\begin{aligned}{\rm Cov}(\hat{b}_{123}\,,\hat{b}_{1'2'3'}) = \frac{1}{N_{123}\,N_{1'2'3'}}\sum_{m_{123},m'_{123}} G_{123}\,G_{1'2'3'}\\ \left(\langle a_1 a_2 a_3 a_{1'} a_{2'} a_{3'}\rangle - \langle a_1 a_2 a_3\rangle\langle a_{1'} a_{2'} a_{3'}\rangle\right).\end{aligned} \tag{B3}$$

When the field is close to Gaussian, the 6-point correlation function can be computed with Wick's theorem (Wick 1950; Komatsu et al. 2002, and references therein)

$$\langle a_1 a_2 a_3 a_{1'} a_{2'} a_{3'}\rangle = (C_\ell)_{123}\,\delta_{1^*,1'}\,\delta_{2^*,2'}\,\delta_{3^*,3'} + 14\ \text{permutations}, \tag{B4}$$

where $\delta_{i^*,j} = (-1)^{m_i}\delta_{\ell_i,\ell_j}\delta_{-m_i,m_j}$.

The 15 permutations of (1, 2, 3, 1′, 2′, 3′) are listed below along with their contribution $\delta$Cov to the covariance:

$$(1^*2)(3^*1')(2'^*3') \to \delta{\rm Cov} = 0 \text{ except if } \ell_3=\ell'_1=0 \tag{B5}$$

$$(1^*2)(3^*2')(1'^*3') \to \delta{\rm Cov} = 0 \text{ except if } \ell_3=\ell'_2=0 \tag{B6}$$

$$(1^*2)(3^*3')(1'^*2') \to \delta{\rm Cov} = 0 \text{ except if } \ell_3=\ell'_3=0 \tag{B7}$$

$$(1^*3)(2^*1')(2'^*3') \to \delta{\rm Cov} = 0 \text{ except if } \ell_2=\ell'_1=0 \tag{B8}$$

$$(1^*3)(2^*2')(1'^*3') \to \delta{\rm Cov} = 0 \text{ except if } \ell_2=\ell'_2=0 \tag{B9}$$

$$(1^*3)(2^*3')(1'^*2') \to \delta{\rm Cov} = 0 \text{ except if } \ell_2=\ell'_3=0 \tag{B10}$$

$$(1^*1')(2^*3)(2'^*3') \to \delta{\rm Cov} = 0 \text{ except if } \ell_1=\ell'_1=0 \tag{B11}$$

$$(1^*1')(2^*2')(3^*3') \to \delta{\rm Cov} = \frac{C_{\ell_1}C_{\ell_2}C_{\ell_3}}{N_{123}}\delta_{\ell_1\ell'_1}\,\delta_{\ell_2\ell'_2}\,\delta_{\ell_3\ell'_3} \tag{B12}$$

$$(1^*1')(2^*3')(3^*2') \to \delta{\rm Cov} = \frac{C_{\ell_1}C_{\ell_2}C_{\ell_3}}{N_{123}}\delta_{\ell_1\ell'_1}\,\delta_{\ell_2\ell'_3}\,\delta_{\ell_3\ell'_2} \tag{B13}$$

$$(1^*2')(2^*3)(1'^*3') \to \delta{\rm Cov} = 0 \text{ except if } \ell_1=\ell'_2=0 \tag{B14}$$

$$(1^*2')(2^*1')(3^*3') \to \delta{\rm Cov} = \frac{C_{\ell_1}C_{\ell_2}C_{\ell_3}}{N_{123}}\delta_{\ell_1\ell'_2}\,\delta_{\ell_2\ell'_1}\,\delta_{\ell_3\ell'_3} \tag{B15}$$

$$(1^*2')(2^*3')(3^*1') \to \delta{\rm Cov} = \frac{C_{\ell_1}C_{\ell_2}C_{\ell_3}}{N_{123}}\delta_{\ell_1\ell'_2}\,\delta_{\ell_2\ell'_3}\,\delta_{\ell_3\ell'_1} \tag{B16}$$

$$(1^*3')(2^*3)(1'^*2') \to \delta{\rm Cov} = 0 \text{ except if } \ell_1=\ell'_3=0 \tag{B17}$$

$$(1^*3')(2^*1')(3^*2') \to \delta{\rm Cov} = \frac{C_{\ell_1}C_{\ell_2}C_{\ell_3}}{N_{123}}\delta_{\ell_1\ell'_3}\,\delta_{\ell_2\ell'_1}\,\delta_{\ell_3\ell'_2} \tag{B18}$$

$$(1^*3')(2^*2')(3^*1') \to \delta{\rm Cov} = \frac{C_{\ell_1}C_{\ell_2}C_{\ell_3}}{N_{123}}\delta_{\ell_1\ell'_3}\,\delta_{\ell_2\ell'_2}\,\delta_{\ell_3\ell'_1}. \tag{B19}$$

Here we do not consider bispectrum coefficients with one multipole equal to zero (which amounts to considering the power spectrum times the monopole). So the bispectrum covariance is diagonal and we find

$${\rm Var}(\hat{b}_{123}) = \frac{C_{\ell_1}C_{\ell_2}C_{\ell_3}}{N_{123}}\times\begin{cases}6 & \text{equilateral triangle}\\ 2 & \text{isosceles triangle}\\ 1 & \text{general triangle.}\end{cases} \tag{B20}$$

This paper has been typeset from a TEX/LATEX file prepared by the author.